# On Harmonic Balance Method-based Lagrangian contact formulations for vibro-impact problems

Thibaut Vadcard, Alain Batailly, Fabrice Thouverez

POLYTECHNIQUE MONTRÉAL
UNIVERSITÉ D'INGÉNIERIE

LABORATOIRE D'ANALYSE VIBRATOIRE ET ACOUSTIQUE

# On Harmonic Balance Method-based lagrangian contact formulations for vibro-impact problems

T. Vadcard[1,2], A. Batailly[1], F. Thouverez[2]

**Abstract**

This article assesses two Harmonic Balance Method-based numerical lagrangian strategies for the characterization of the periodic response of a mechanical system subject to unilateral contact constraints. The model used for evaluation is an academic rod model facing an obstacle that is firstly considered as equivalent to a stiffness (flexible) and then as a rigid obstacle. Nonlinear frequency response curves are obtained through an arc-length continuation procedure and confronted to the corresponding time integration simulations. An in-depth comparative analysis is conducted on the time signals obtained through both frequency domain strategies: (1) linear complementarity problem (LCP-HBM) and (2) dynamic lagrangian frequency time (DLFT-HBM). The unilateral contact conditions are thoroughly investigated in the time domain and compared with the reference time integration simulations. Particular attention is paid to the relation between both methods and it is shown that the DLFT-HBM is asymptotically equivalent to the LCP-HBM. This study also shows that the oversampling of time signals inside alternating frequency-time procedures generates non-physical high harmonics. Finally, a convergence analysis is conducted in order to assess the influence of the different numerical parameters on the respect of the unilateral contact laws.

**Keywords**

Harmonic balance method ; Unilateral contact ; Nonsmooth dynamics ; Linear complementarity problem

1 - Department of Mechanical Engineering, École Polytechnique de Montréal, P.O. Box 6079, Succ. Centre-Ville, Montréal, Québec, Canada H3C 3A7
2 - École Centrale de Lyon, Laboratoire de Tribologie et Dynamique des Systèmes, UMR CNRS 5513, 36 avenue Guy de Collongue, Écully, 69134, France

# Formulations lagrangiennes du contact basées sur la méthode de l'équilibrage harmonique pour des problèmes de vibro-impact

T. Vadcard[1,2], A. Batailly[1], F. Thouverez[2]

**Résumé**

Cet article évalue deux stratégies numériques lagrangiennes basées sur la méthode d'équilibrage harmonique pour la caractérisation de la réponse périodique d'un système mécanique sujet à une contrainte de contact unilatéral. Un modèle académique de barre est utilisé, d'abord face à un obstacle consdéré comme une raideur (flexible), puis face à un obstacle rigide. Les courbes de réponse en fréquence sont obtenues grâce à une procédure de continuation par longueur d'arc et elles sont confrontées à des simulations issues de l'intégration temporelle. Une fine étude comparative est réalisée sur les signaux temporels obtenus par les deux méthodes fréquentielles : (1) le problème de complémentarité linéaire (LCP-HBM) et (2) la *dynamic lagrangian frequency time* (DLFT-HBM). Le respect des conditions de contact unilatéral est soigneusement étudié dans le domaine temporel et comparé avec les solutions de référence de l'intégration temporelle. une attention particulière est portée à la relation entre les deux méthodes fréquentielles et il est montré que la DLFT-HBM est asymptotiquement équivalente à la LCP-HBM. Cette étude montre également que le suréchantillonnage des signaux temporels au sein des procédures d'alternance fréquence-temps génère des harmoniques non-physiques d'ordre haut. Finalement, une étude de convergence est conduite pour évaluer l'influence des différents paramètres numériques sur le respect de la loi de contact unilatéral.

**Mots-clés**

Méthode d'équilibrage harmonique ; Contact unilatéral ; Dynamique non-régulière ; Problème de complémentarité linéaire

1 - Département de génie mécanique, École Polytechnique de Montréal, P.O. Box 6079, Succ. Centre-Ville, Montréal, Québec, Canada H3C 3A7
2 - École Centrale de Lyon, Laboratoire de Tribologie et Dynamique des Systèmes, UMR CNRS 5513, 36 avenue Guy de Collongue, Écully, 69134, France

## 1 Introduction

The field of nonsmooth dynamics in mechanics refers to the description of problems whose solutions are not twice differentiable in time, *i.e* featuring discontinuities at singular instants. Two types of situations are usually encountered: acceleration discontinuities for example for the stick-slip phenomenon in friction-induced vibrations problems [21] and velocity discontinuities for vibro-impact problems [1]. The latter are being adressed in this paper. This subject of research is highly active, as shown by the wide variety of predictive numerical strategies developed to accurately describe contact interactions [1, 4, 6, 16, 18, 21, 23, 26, 27, 33, 34, 35]. Time marching strategies [4, 16, 27, 33, 34] are usually privileged since they only require few approximations on the solutions. Actually, they provide a good insight on both transient and steady state behaviours. However, the associated high computational cost makes this type of strategies ill-suited for the research of periodic solutions. When such solutions are investigated, other solution methods, such as the harmonic balance method (HBM) may be used in a more effective way without relying on initial conditions. Though, it is well known that the Fourier basis provides a poor approximation of nonsmooth functions which constitutes a roadblock for the application of HBM to nonsmooth mechanical systems. The wavelet Galerkin procedure [17, 37] has proven to provide a good estimation of contact forces if the wavelet family is properly chosen. Mixed approaches are also possible by coupling a family of Fourier functions with several wavelet functions [21]. An hybrid approach coupling the shooting method and the HBM was also developed in order to characterize vibro-impact systems with friction [41]. The HBM is used throughout this paper since it is more versatile and does not require a choice of a wavelet functions beforehand.

The HBM privileged industrial applications are systems that are under periodic external loadings. In fact, it was initially developed to tackle nonlinear periodic oscillations of electronic circuits [12, 30]. Another typical application of the HBM may be found in the field of turbomachinery where the whole system is under periodic aerodynamic and mechanical forcing due to the rotation of the shafts. Therefore, it is widely used on industrial applications in the field of nonlinear dynamics applied to bladed disks in terms of friction damping [**petrov˙high-accuracy˙2010**, 29, 47], geometric nonlinearities [14, 25] and rubbing interactions [6, 38]. The methodologies allowing to account for nonlinearities in numerical simulations are usually classified according to the type of nonlinearity at stake. Thus, it usually makes it difficult to conduct simulations with several types of nonlinearities because of the wide variety of strategies. Therefore, this paper is based on an HBM approach which has proven its efficiency for friction applications, and for which it is shown that it may be also considered for vibro-impact configurations. The use of this common strategy will allow to account for both tip/casing interactions as well as friction damping in further calculations. As a first step towards this goal, the study presented in this article uses an academical vibro-impact system allowing to finely evaluate the performances of the methodology without any restrictions on the domain of application.

Contact nonlinearities associated with the HBM come with a difficulty inherent to the frequency formulations: Coulomb's law and Hertz-Signorini-Moreau conditions must be applied in the time domain, thus standard strategies to evaluate the nonlinear contact forces are a part of an Alternating Frequency-Time (AFT) procedure [2, 3, 6, 7, 15, 20, 29, 36, 39, 42, 43], the AFT procedure was assessed in [43] on both smooth and nonsmooth applications. The nonsmooth behaviour of contact interactions has widely been studied by means of the HBM. For instance, the HBM was used on phenomenological nonsmooth systems in order to observe sophisticated behaviours such as quasi-periodic orbits [7, 36], sub-harmonic and super-harmonic resonances [2, 9, 20], detached solution branches [2, 11, 15] or vibration localization [11, 31]. Several methodologies have also been developped in order to compute solutions to nonsmooth problems based on the HBM, without relying on an the AFT scheme. One may state the asymptotic numerical method [18], the linear complementarity problem formulation proposed in [26] and the event-driven strategy suggested in [23].

When it comes to unilateral contact, several contact treatments exist in order to compute nonlinear forces. A large majority of the methodologies rely on a penalty-based contact treatment [2, 6, 7, 9, 11, 18, 20, 23, 31, 36, 43, 44]. For some applications, the latter being too challenging from a numerical standpoint, an additional regularization is added [6, 18, 43, 44] to smoothen the nonsmoothness of contact forces. To the contrary, the Dynamical Lagrangian Frequency-Time associated with HBM (DLFT-HBM) directly simulates the unilateral contact law [29] without requiring a penalty-based contact treatement. The latter is widely used for computing friction-damped frequency responses [5, 15, 29, 40]. However, very few calculations were made in a stiff unilateral contact context, except for a

phenomenological model [28]. Hence, this article focuses on assessing the DLFT-HBM for a vibro-impact problem.

Many research works suggest a new approach when it comes to unilateral contact constraints [1, 16, 26, 27, 46]: the linear complementarity problems (LCP) are composed of a set of linear algebraic equations whose variables are subject to inequalities and complementarity conditions. This family of problem is particularly well suited for contact interactions since they can include the unilateral complementarity conditions as part of the whole constrained problem. These problems are solved through dedicated solvers that can be of different nature: (1) pivotal [24] and (2) iterative (Newton-like) [10]. These algorithms were initially developed for game theory [24], and more recently applied to nonsmooth dynamics. In the field of contact dynamics, the LCP is mainly used at each time step in time-marching strategies [16, 27, 46]. However, the periodicity assumption of the HBM allows to consider a high-dimension LCP over the whole period, as shown in [26]. Since the solutions to these problems strictly respect the unilateral contact constraints, they provide a new comparison basis in the HBM framework.

With the intent of providing multiple solutions to the same problem with different methods in order to precisely identify differences between them and the reference solution, this paper presents and assesses two HBM-based strategies to find periodic solutions to the equation of motion subject to unilateral contact constraints: the DLFT-HBM and a LCP formulation of the HBM (LCP-HBM). In Sec. 2, both formulations are thoroughly derived and precise descriptions are given for a better understanding of these methodologies. The rod model test case is then presented in Sec. 3. The numerical behaviours of both harmonic methodologies with contact conditions are presented for comparison with the unilateral law. Finally, in Sec. 4 the DLFT-HBM is pushed to its limits and a critical viewpoint is given on the interpretation of AFT time signals.

## 2 Lagrangian contact harmonic balance method

This section aims to present all the theoretical and methodological elements required for the understanding and implementation of the lagrangian contact harmonic balance methods exposed in this paper.

The nonlinear equation of motion for a $n$-dof (degrees of freedom) system with respect to time reads:

$$\mathbf{M}\ddot{\mathbf{x}}(t) + \mathbf{C}\dot{\mathbf{x}}(t) + \mathbf{K}\mathbf{x}(t) + \mathbf{f}_{\text{nl}}(\mathbf{x}(t), \dot{\mathbf{x}}(t)) = \mathbf{f}_{\text{ex}}(\omega, t) \tag{1}$$

where $\mathbf{x}$ is the unknown displacement field, $\mathbf{M}$, $\mathbf{C}$ and $\mathbf{K}$ respectively stand for the mass, damping and stiffness matrices, $\mathbf{f}_{\text{nl}}$ is the nonlinear contact forces vector and $\mathbf{f}_{\text{ex}}$ is an external periodic excitation of fundamental angular pulsation $\omega$. The overdots refer to time derivatives. In the case of contact interactions, nonlinear forces and gap constraints are subject to complementarity conditions as well as inequalities. In order to find a solution to a contact problem, nonlinear forces must be computed such that Hertz-Signorini-Moreau conditions or Unilateral Contact Constraints (UCC) are respected. These conditions on a single contact constraint read [1]:

$$\lambda(t) \geq 0 \qquad g(t) \geq 0 \qquad \lambda(t)g(t) = 0 \tag{2}$$

where $\lambda(t)$ is the contact force in the normal direction and $g(t)$ the gap function. These three conditions are usually rewritten in the compact form on time-discretized vectors:

$$\mathbf{0} \leq \boldsymbol{\lambda} \perp \mathbf{g} \geq \mathbf{0} \tag{3}$$

### 2.1 Harmonic balance method

Excitation forces, that are assumed periodic may be approximated with a truncated Fourier series with $N_{\text{h}}$ harmonics:

$$\mathbf{f}_{\text{ex}}(t) \simeq \frac{1}{2}\mathbf{a}_0^{\text{ex}} + \sum_{k=1}^{N_{\text{h}}} \left(\mathbf{a}_k^{\text{ex}} \cos(k\omega t) + \mathbf{b}_k^{\text{ex}} \sin(k\omega t)\right) \tag{4}$$

where $\mathbf{a}_k^{\text{ex}}$ and $\mathbf{b}_k^{\text{ex}}$ are known *a priori*. Usually, the excitation is considered monoharmonic and the only non-zero coefficients are $\mathbf{a}_1^{\text{ex}}$ and $\mathbf{b}_1^{\text{ex}}$.

Assuming the solution displacement $\mathbf{x}$ and nonlinear forces $\mathbf{f}_{\text{nl}}$ are periodic with the same period as the excitation forces $\mathbf{f}_{\text{ex}}$, both quantities can also be approximated by truncated Fourier series Eq. (4):

$$\mathbf{x}(t) \simeq \frac{1}{2}\mathbf{a}_0 + \sum_{k=1}^{N_\text{h}} \left(\mathbf{a}_k \cos(k\omega t) + \mathbf{b}_k \sin(k\omega t)\right) \tag{5}$$

$$\mathbf{f}_{\text{nl}}(t) \simeq \frac{1}{2}\mathbf{a}_0^{\text{nl}} + \sum_{k=1}^{N_\text{h}} \left(\mathbf{a}_k^{\text{nl}} \cos(k\omega t) + \mathbf{b}_k^{\text{nl}} \sin(k\omega t)\right) \tag{6}$$

where $\mathbf{a}_k$, $\mathbf{b}_k$, $\mathbf{a}_k^{\text{nl}}$ and $\mathbf{b}_k^{\text{nl}}$ are the real Fourier coefficients: the new unknowns of the problem. The choice of $N_\text{h}$ is made such that the contact forces $\mathbf{f}_{\text{nl}}(t)$ as well as the correponding response in terms of displacements are accurately described. Unlike the excitation forces, all the coefficients are generally non-zero because of the nonlinear phenomena. All the $\mathbf{a}_k^\bullet$ and $\mathbf{b}_k^\bullet$ where $\bullet = \{-, \text{nl}, \text{ex}\}$ are vectorial of dimension $n$ and read:

$$\begin{cases} \mathbf{a}_k^\bullet = [a_k^{\bullet,1}, a_k^{\bullet,2}, \dots, a_k^{\bullet,n}]^\top \text{ for } k \in [\![0; N_\text{h}]\!] & (7) \\ \mathbf{b}_k^\bullet = [b_k^{\bullet,1}, b_k^{\bullet,2}, \dots, b_k^{\bullet,n}\ ]^\top \text{ for } k \in [\![1; N_\text{h}]\!] & (8) \end{cases}$$

In order to simplify expressions, all Fourier coefficients are concatenated in $n(2N_\text{h}+1)$-dimensional vectors such as:

$$\widetilde{\mathbf{x}} = [\frac{1}{2}\mathbf{a}_0^\top\ \mathbf{a}_1^\top\ \mathbf{b}_1^\top \dots\ \mathbf{a}_{N_\text{h}}^\top\ \mathbf{b}_{N_\text{h}}^\top]^\top \tag{9}$$

$$\widetilde{\mathbf{f}}_{\text{nl}} = [\frac{1}{2}(\mathbf{a}_0^{\text{nl}})^\top\ (\mathbf{a}_1^{\text{nl}})^\top\ (\mathbf{b}_1^{\text{nl}})^\top \dots\ (\mathbf{a}_{N_\text{h}}^{\text{nl}})^\top\ (\mathbf{b}_{N_\text{h}}^{\text{nl}})^\top]^\top \tag{10}$$

$$\widetilde{\mathbf{f}}_{\text{ex}} = [\frac{1}{2}(\mathbf{a}_0^{\text{ex}})^\top\ (\mathbf{a}_1^{\text{ex}})^\top\ (\mathbf{b}_1^{\text{ex}})^\top \dots\ (\mathbf{a}_{N_\text{h}}^{\text{ex}})^\top\ (\mathbf{b}_{N_\text{h}}^{\text{ex}})^\top]^\top \tag{11}$$

The $\widetilde{\bullet}$ notation refers to multiharmonic vectors. By introducing $\mathbf{B}$ as the real Fourier functions basis such as:

$$\mathbf{B}(t) = [\frac{1}{2},\ \cos(\omega t),\ \sin(\omega t),\ \dots,\ \cos(N_\text{h}\omega t),\ \sin(N_\text{h}\omega t)]^\top \tag{12}$$

It is possible to rewrite the Fourier series Eqs. (4) to (6) as follows:

$$\mathbf{x}(t) = (\mathbf{B}(t) \otimes \mathbf{I}_n)\widetilde{\mathbf{x}} \tag{13}$$

$$\mathbf{f}_{\text{nl}}(t) = (\mathbf{B}(t) \otimes \mathbf{I}_n)\widetilde{\mathbf{f}_{\text{nl}}} \tag{14}$$

$$\mathbf{f}_{\text{ex}}(t) = (\mathbf{B}(t) \otimes \mathbf{I}_n)\widetilde{\mathbf{f}_{\text{ex}}} \tag{15}$$

And by deriving this expression with respect to time $t$, it is possible to obtain velocities and accelerations:

$$\dot{\mathbf{x}}(t) = (\dot{\mathbf{B}}(t) \otimes \mathbf{I}_n)\widetilde{\mathbf{x}} = ((\boldsymbol{\nabla}\mathbf{B})(t) \otimes \mathbf{I}_n)\widetilde{\mathbf{x}} \tag{16}$$

$$\ddot{\mathbf{x}}(t) = (\ddot{\mathbf{B}}(t) \otimes \mathbf{I}_n)\widetilde{\mathbf{x}} = ((\boldsymbol{\nabla}^2\mathbf{B})(t) \otimes \mathbf{I}_n)\widetilde{\mathbf{x}} \tag{17}$$

where $\boldsymbol{\nabla}$ is the derivative operator for the basis $\mathbf{B}$ defined as:

$$\boldsymbol{\nabla} = \text{blockdiag}(\mathbf{0},\ \boldsymbol{\nabla}_1,\ \dots,\ \boldsymbol{\nabla}_{N_\text{h}}) \text{ and } \boldsymbol{\nabla}^2 = \boldsymbol{\nabla}\boldsymbol{\nabla} \tag{18}$$

with the elementary derivative block $\boldsymbol{\nabla}_k$:

$$\boldsymbol{\nabla}_k = \begin{pmatrix} 0 & k\omega \\ -k\omega & 0 \end{pmatrix} \quad \forall k \in [\![1, N_\text{h}]\!] \tag{19}$$

Thanks to the $\mathbf{B}$ basis, it is possible to define the Inverse Discrete Fourier Transform (IDFT) matrix $\overline{\mathcal{F}}$ that allows to compute discretized time signals of size $N_\mathrm{t}$ given the multiharmonic vectors,

$$\overline{\mathcal{F}} = \left( (\mathbf{B}(t_1) | \dots | \mathbf{B}(t_i) | \dots | \mathbf{B}(t_{N_\mathrm{t}}))^\top \right) \otimes \mathbf{I}_n \tag{20}$$

the Discrete Fourier Transform (DFT) matrix $\mathcal{F}$ can be expressed as its Moore-Penrose pseudo-inverse:

$$\mathcal{F} = \overline{\mathcal{F}}^\top \left( \overline{\mathcal{F}} . \overline{\mathcal{F}}^\top \right)^{-1} \tag{21}$$

The Fourier matrices are mainly used to switch between the time domain and the frequency domain, such that,

$$\widetilde{\bullet} = \mathcal{F} \left\{ \bullet(t_i) \right\}_{i=1\dots N_\mathrm{t}} \qquad \left\{ \bullet(t_i) \right\}_{i=1\dots N_\mathrm{t}} = \overline{\mathcal{F}} \widetilde{\bullet} \tag{22}$$

The substitution of the truncated Fourier series and its derivatives Eqs. (9), (10), (11), (16), (17) in Eq. (1) followed by a Fourier-Galerkin projection yields $n(2N_\mathrm{h}+1)$ nonlinear algebraic equations in the frequency domain:

$$\mathcal{H}(\widetilde{\mathbf{x}}, \omega) = \mathbf{Z}(\omega)\widetilde{\mathbf{x}} + \widetilde{\mathbf{f}}_\mathrm{nl}(\widetilde{\mathbf{x}}) = \widetilde{\mathbf{f}}_\mathrm{ex} \tag{23}$$

where $\mathbf{Z}(\omega)$ is a block diagonal matrix, referred to as the dynamic stiffness matrix whose $N_\mathrm{h}+1$ blocks are defined as follows:

$$\mathbf{Z}_0 = \mathbf{K} \quad \text{and} \quad \mathbf{Z}_k(\omega) = \begin{pmatrix} \mathbf{K} - (k\omega)^2\mathbf{M} & k\omega\mathbf{C} \\ -k\omega\mathbf{C} & \mathbf{K} - (k\omega)^2\mathbf{M} \end{pmatrix} \quad \forall k \in [\![1, N_\mathrm{h}]\!] \tag{24}$$

The nonlinear dependence of $\widetilde{\mathbf{f}}_\mathrm{nl}$ on $\widetilde{\mathbf{x}}$ makes Eq. (23) nonlinear. It is thus necessary to solve it through an iterative method. These methods are usually based on Newton-Raphson or pseudo-Newton algorithms [32]. In this article, the Newton-Raphson algorithm is used to compute the solutions to the HBM nonlinear problem.

### 2.2 Harmonic balance equation condensation

The algebraic formulation of the truncated equation of motion allows to use two exact condensation procedures in order to reduce the size of the nonlinear problem, and thus the computation times. The first condensation procedure aims to retain only the nonlinear dof in the resolution and the second condensation allows to divide the size of the nonlinear harmonic system by two by associating the nonlinear dof of each structure in pairs.

#### Condensation of linear dof

Among the $n$ dof, it is possible to separate the nonlinear dof that withstand nonlinear forces from the other dof, referred to as linear. These two sets of dof are respectively identified by the subscripts nl and L. The fact that there are no nonlinear forces on linear dof, $\widetilde{\mathbf{x}}_\mathrm{L}$ can be expressed through Eq. (25) such as:

$$\begin{pmatrix} \mathbf{Z}_{\mathrm{L,L}} & \mathbf{Z}_{\mathrm{L,nl}} \\ \mathbf{Z}_{\mathrm{nl,L}} & \mathbf{Z}_{\mathrm{nl,nl}} \end{pmatrix} \begin{pmatrix} \widetilde{\mathbf{x}}_\mathrm{L} \\ \widetilde{\mathbf{x}}_\mathrm{nl} \end{pmatrix} + \begin{pmatrix} \mathbf{0} \\ \widetilde{\mathbf{f}}_\mathrm{nl} \end{pmatrix} = \begin{pmatrix} \widetilde{\mathbf{f}}_{\mathrm{ex,L}} \\ \widetilde{\mathbf{f}}_{\mathrm{ex,nl}} \end{pmatrix} \tag{25}$$

$$\widetilde{\mathbf{x}}_\mathrm{L} = \mathbf{Z}_{\mathrm{L,L}}^{-1} \left( \widetilde{\mathbf{f}}_{\mathrm{ex,L}} - \mathbf{Z}_{\mathrm{L,nl}} \widetilde{\mathbf{x}}_\mathrm{nl} \right) \tag{26}$$

The substitution of $\widetilde{\mathbf{x}}_\mathrm{L}$ into Eq. (25) leads to the following expression:

$$\mathbf{Z}_\mathrm{red} \widetilde{\mathbf{x}}_\mathrm{nl} + \widetilde{\mathbf{f}}_{\mathrm{nl,red}} = \widetilde{\mathbf{f}}_{\mathrm{ex,red}} \tag{27}$$

where:

$$\mathbf{Z}_{\text{red}} = \mathbf{Z}_{\text{nl,nl}} - \mathbf{Z}_{\text{nl,L}}\mathbf{Z}_{\text{L,L}}^{-1}\mathbf{Z}_{\text{L,nl}} \tag{28}$$

$$\widetilde{\mathbf{f}}_{\text{ex,red}} = \widetilde{\mathbf{f}}_{\text{ex,nl}} - \mathbf{Z}_{\text{nl,L}}\mathbf{Z}_{\text{L,L}}^{-1}\widetilde{\mathbf{f}}_{\text{ex,L}} \tag{29}$$

$$\widetilde{\mathbf{f}}_{\text{nl,red}} = \widetilde{\mathbf{f}}_{\text{nl}} \tag{30}$$

The harmonic system being condensed on the nonlinear dof, its size becomes $n_{\text{nl}}(2N_{\text{h}}+1)$ equations with $n_{\text{nl}}$ being the number of nonlinear dof. The $\mathbf{Z}_{\text{red}}$ matrix is in fact the Schur complement to the $\mathbf{Z}_{\text{L,L}}$ block of the matrix $\mathbf{Z}$.

### Condensation of relative nonlinear dof

In the framework of contact interactions, two structures are generally involved. Moreover, contact laws are formulated with the so-called gap function $g$ (and its first derivative with respect to time, the relative speed), resulting from the distance between both structures, also called relative displacement $x_{\text{r}}$ in some applications. In the case of co-located nodes, it is possible to write the gap function as $g(t) = x_{\text{r}}(t) = x^1(t) - x^2(t)$ where $x^1$ and $x^2$ respectively refer to the nonlinear dof for the first and the second structure. This gap expression only stays valid if the nodes associated with $x^1$ and $x^2$ are facing each other, this is particularly true for unidimensional configurations because no misalignment can occur (contrarily with 2D and 3D applications). This configuration is illustrated with 1D structures on Fig. 1.

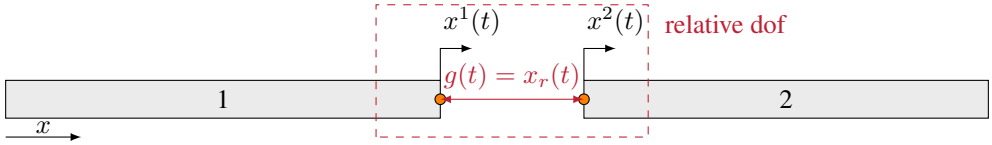


**Figure 1.** Representation of the relative dof formalism in 1D.

We may note that the contact forces involved in an interaction are reciprocal. Due to the latter property of contact interactions and the algebraic nature of the HBM nonlinear system of equations, it is possible to formulate a condensed problem where the multiharmonic vector of relative nonlinear displacement $\widetilde{\mathbf{x}}_{\text{r}} = \mathcal{F}\mathbf{g} = \mathcal{F}\mathbf{x}_{\text{r}}$ is the new unknown of the problem. This exact condensation yields a significant computation speed up since it divides the size of the nonlinear system Eq. (27) by a factors two. Without this condensation step, it would be necessary to solve the equilibrium on both structures 1 and 2 at the same time, whereas the condensed system only requires to solve one equation per pair of nonlinear dof. The new unknown is written as:

$$\widetilde{\mathbf{x}}_{\text{r}} = \widetilde{\mathbf{x}}_{\text{nl}}^1 - \widetilde{\mathbf{x}}_{\text{nl}}^2 \tag{31}$$

In order to perform the condensation on relative nonlinear dof, it is necessary to partition the system equation into two parts, each part being related to one of the two structures.

$$\mathbf{Z}_{\text{red}}^1\widetilde{\mathbf{x}}_{\text{nl}}^1 + \widetilde{\mathbf{f}}_{\text{nl,red}}^1\left(\widetilde{\mathbf{x}}_{\text{nl}}^1, \widetilde{\mathbf{x}}_{\text{nl}}^2\right) = \widetilde{\mathbf{f}}_{\text{ex,red}}^1 \tag{32a}$$

$$\mathbf{Z}_{\text{red}}^2\widetilde{\mathbf{x}}_{\text{nl}}^2 + \widetilde{\mathbf{f}}_{\text{nl,red}}^2\left(\widetilde{\mathbf{x}}_{\text{nl}}^1, \widetilde{\mathbf{x}}_{\text{nl}}^2\right) = \widetilde{\mathbf{f}}_{\text{ex,red}}^2 \tag{32b}$$

The third law of Newton naturally implies:

$$\widetilde{\mathbf{f}}_{\text{nl,red}}^1\left(\widetilde{\mathbf{x}}_{\text{nl}}^1, \widetilde{\mathbf{x}}_{\text{nl}}^2\right) = -\widetilde{\mathbf{f}}_{\text{nl,red}}^2\left(\widetilde{\mathbf{x}}_{\text{nl}}^1, \widetilde{\mathbf{x}}_{\text{nl}}^2\right) = \widetilde{\mathbf{f}}_{\text{nl,r}} \tag{33}$$

By multiplying Eq. (32a) by $\left(\mathbf{Z}_{\text{red}}^1\right)^{-1}$ and Eq. (32b) by $\left(\mathbf{Z}_{\text{red}}^2\right)^{-1}$, using the reciprocity of the contact forces Eq. (33) and then substracting one equation with the other gives Eq. (34):

$$\widetilde{\mathbf{x}}_{\text{nl}}^1 - \widetilde{\mathbf{x}}_{\text{nl}}^2 + \left(\left(\mathbf{Z}_{\text{red}}^1\right)^{-1} + \left(\mathbf{Z}_{\text{red}}^2\right)^{-1}\right)\widetilde{\mathbf{f}}_{\text{nl,r}} = \left(\mathbf{Z}_{\text{red}}^1\right)^{-1}\widetilde{\mathbf{f}}_{\text{ex,red}}^1 - \left(\mathbf{Z}_{\text{red}}^2\right)^{-1}\widetilde{\mathbf{f}}_{\text{ex,red}}^2 \tag{34}$$

It is then possible to multiply Eq. (34) by $\mathbf{Z}_\mathrm{r} = \left( \left(\mathbf{Z}^1_\mathrm{red}\right)^{-1} + \left(\mathbf{Z}^2_\mathrm{red}\right)^{-1} \right)^{-1}$ in order to retrieve the classical form of the HBM equilibrium system:

$$\mathbf{Z}_\mathrm{r} \left( \widetilde{\mathbf{x}}^1_\mathrm{nl} - \widetilde{\mathbf{x}}^2_\mathrm{nl} \right) + \widetilde{\mathbf{f}}_\mathrm{nl,r} = \mathbf{Z}_\mathrm{r} \left( \left(\mathbf{Z}^1_\mathrm{red}\right)^{-1} \widetilde{\mathbf{f}}^1_\mathrm{ex,red} - \left(\mathbf{Z}^2_\mathrm{red}\right)^{-1} \widetilde{\mathbf{f}}^2_\mathrm{ex,red} \right) \tag{35}$$

The condensed external forces term $\widetilde{\mathbf{f}}_\mathrm{ex,r}$ can be identified:

$$\widetilde{\mathbf{f}}_\mathrm{ex,r} = \mathbf{Z}_\mathrm{r} \left( \left(\mathbf{Z}^1_\mathrm{red}\right)^{-1} \widetilde{\mathbf{f}}^1_\mathrm{ex,red} - \left(\mathbf{Z}^2_\mathrm{red}\right)^{-1} \widetilde{\mathbf{f}}^2_\mathrm{ex,red} \right) \tag{36}$$

The final system condensed on the nonlinear relative dof is as follows:

$$\mathbf{Z}_\mathrm{r} \widetilde{\mathbf{x}}_\mathrm{r} + \widetilde{\mathbf{f}}_\mathrm{nl,r}(\widetilde{\mathbf{x}}_\mathrm{r}) = \widetilde{\mathbf{f}}_\mathrm{ex,r} \tag{37}$$

The final size of the harmonic system is $\frac{n_\mathrm{nl}}{2}(2N_\mathrm{h}+1)$. It is worth noting that the two reductions steps presented do not lead to any approximation of the system's dynamic. However, the numerical quality of $\mathbf{Z}_\mathrm{r}$ and $\widetilde{\mathbf{f}}_\mathrm{ex,r}$ may be affected since their expressions involve matrix inversions thus introducing numerical errors.

#### Retrieval of the results on linear dof

These condensation techniques imply the use of additional post-processing steps in order to retrieve the results on the whole structure. When the condensed problem is solved, $\widetilde{\mathbf{f}}_\mathrm{nl,r}$ can be computed by means of Eq. (37) thanks to the knowledge of a solution $\widetilde{\mathbf{x}}_\mathrm{r}$ in terms of relative displacement. The contact forces multiharmonic vector can then be substituted in the full system's equilibrium Eq. (25) to linearly solve for $\widetilde{\mathbf{x}}$ containing the solution for every dof of the system.

### 2.3 Alternating frequency-time procedure

The Alternating Frequency-Time (AFT) scheme is widely used for all types of nonlinearities in a HBM framework [3, 6, 8, 13, 15, 29, 36, 38, 43]. The AFT method consists in going back and forth between the time and frequency domains as a part of an iterative Newton-Raphson procedure. At each iteration of the optimization algorithm, an iterate of the multiharmonic vector of unknown $\widetilde{\mathbf{x}}$ is available, say $\widetilde{\mathbf{x}}^k$ at iteration $k$. Since the laws governing nonlinearities are usually tailored for the time domain, the iterate $\widetilde{\mathbf{x}}^k$ is used to compute the time-discretized signals associated by means of an IDFT: $\mathbf{X}^k = \left\{ \mathbf{x}^k(t_i) \right\}_{i=1\dots N_\mathrm{t}} = \overline{\mathcal{F}} \widetilde{\mathbf{x}}^k$ and $\dot{\mathbf{X}}^k = \left\{ \dot{\mathbf{x}}^k(t_i) \right\}_{i=1\dots N_\mathrm{t}} = \overline{\mathcal{F}} \boldsymbol{\nabla} \widetilde{\mathbf{x}}^k$. The time signals allow to compute the nonlinear forces such as $\mathbf{f}^k_\mathrm{nl}(t) = \boldsymbol{f}(\mathbf{x}^k, \dot{\mathbf{x}}^k)$ where $\boldsymbol{f}(\bullet, \dot{\bullet})$ is a nonlinear analytical function that links displacements and velocities to nonlinear forces. Usually $\boldsymbol{f}$ cannot be easily expressed in the frequency domain, thus justifying the use of the AFT scheme. As a last step, the multiharmonic vector of nonlinear forces is computed through a DFT of the time signal of nonlinear forces $\widetilde{\mathbf{f}}^k_\mathrm{nl} = \mathcal{F} \left\{ \mathbf{f}^k_\mathrm{nl}(t_i) \right\}_{i=1\dots N_\mathrm{t}}$, the knowledge of the latter is enough to perform the computation of the HBM residual and to go on in the Newton-Raphson procedure. An illustration of the AFT scheme is shown in Fig. 2 for a polynomial nonlinearity.

When using the AFT scheme, time domain signals are discretized. One should pay particular attention to this discretization: the Nyquist-Shannon criterion must be respected. Given $N_\mathrm{h}$ harmonics, time signals must be composed of at least $N_\mathrm{t} = 2N_\mathrm{h}+1$ time instants in order not to lose any information through Fourier transforms. Two key concepts are defined below in order to understand more finely the influence of the time discretization on the methodology:

**oversampling:** one of the main features of nonsmooth applications lies in the presence of velocity and acceleration discontinuities. In order to precisely detect these discontinuities through the AFT, a large number $N_\mathrm{t}$ of time instants must be considered within the time domain thus yielding an oversampling of time signals.

**truncature:** as a consequence of the oversampling, contact forces can contain harmonic contributions up to a maximum frequency of $\omega_\mathrm{max} = \frac{N_\mathrm{t} N_\mathrm{h}}{2N_\mathrm{h}+1}\omega$. However, since the HBM resolution is limited to frequencies below $N_\mathrm{h}\omega$, the harmonics of higher order are truncated when going back to the frequency domain.

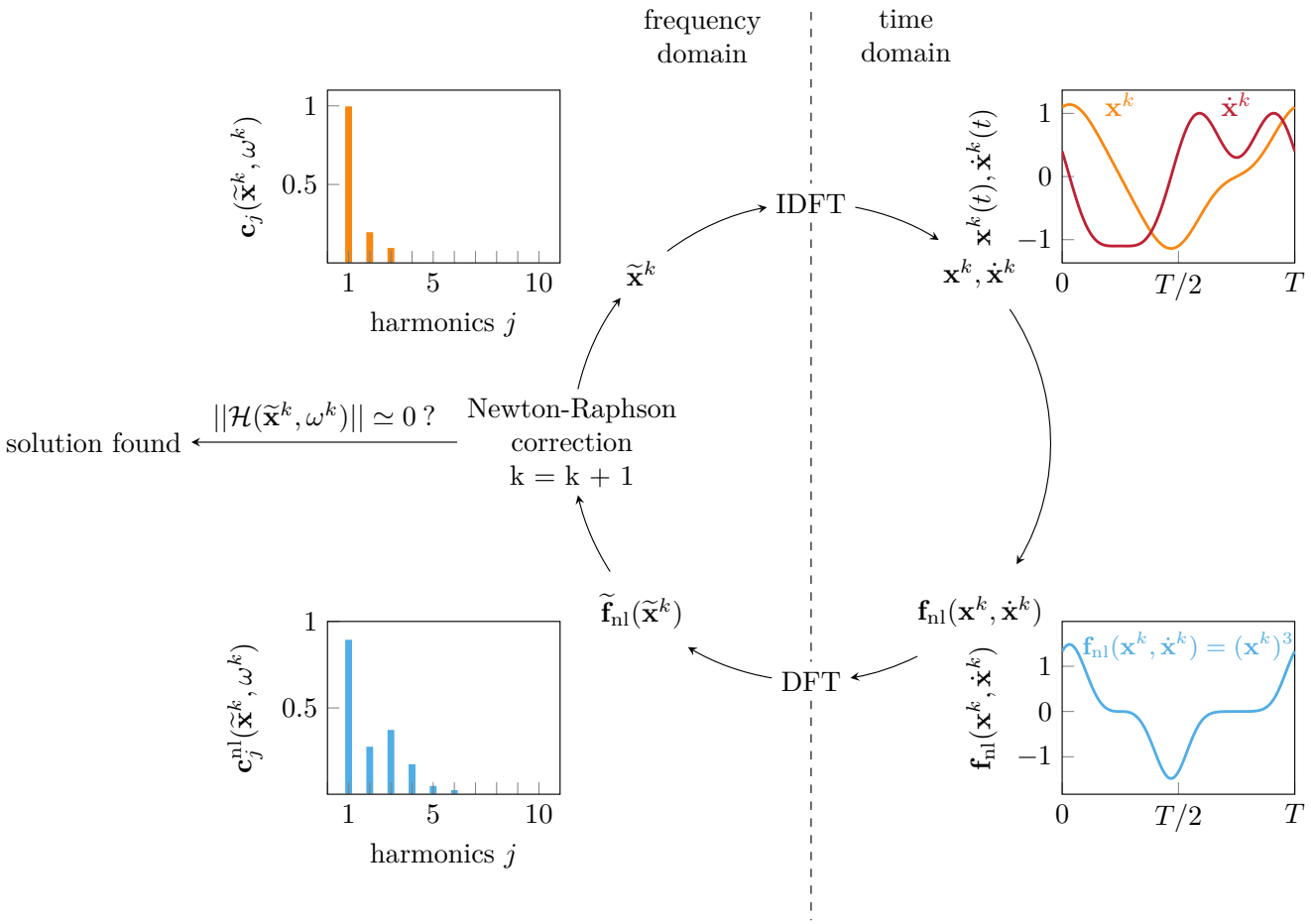


**Figure 2.** AFT procedure for a cubic nonlinearity $f_{\mathrm{nl}}(x) = x^3$ (adapted from [6, 22]).

In the following article, the HBM bandwidth refers to frequency range used in the HBM resolution: frequential contributions below $N_{\mathrm{h}}\omega$. In the end, the AFT procedure can be interpreted as a step of oversampling of the time domain signals followed by a step of truncature (or filtering) of the harmonics beyond the HBM bandwidth contained in the nonsmooth forces. These two aspects come together since the high order harmonics are a direct consequence of the oversampling.

### 2.4 Dynamic Lagrangian Frequency-Time

The Dynamic Lagrangian Frequency-Time associated with the HBM (DLFT-HBM) [29] is a methodology based on the AFT strategy used to deal with contact interactions, such as dry friction and unilateral contact. These nonlinearities cannot be dealt with a simple AFT procedure since the forces cannot be written as analytical expressions in the time domain. The DLFT-HBM is in fact an alternative version of the AFT strategy where the workflow is modified in order to make it possible to compute contact forces without analytical expressions.

#### 2.4.1 General overview

As a starting point, the condensed equation of motion used for DLFT-HBM is written as a reminder:

$$\mathcal{H}_{\mathrm{r}}(\widetilde{\mathbf{x}}_{\mathrm{r}}) = \mathbf{Z}_{\mathrm{r}}\widetilde{\mathbf{x}}_{\mathrm{r}} + \widetilde{\boldsymbol{\lambda}}(\widetilde{\mathbf{x}}_{\mathrm{r}}) - \widetilde{\mathbf{f}}_{\mathrm{ex,r}} = \mathbf{0} \tag{38}$$

For this paper, the quantities of interest $\widetilde{\mathbf{x}}_\mathrm{r}$, $\widetilde{\boldsymbol{\lambda}}$ and $\widetilde{\mathbf{f}}_{\mathrm{ex,r}}$ are along the normal direction in order to model unilateral contact, and tangential directions are ommited. All the equations presented in this section consider a single nonlinear relative dof, the extension to several contact nodes is straight-forward and thus not developped here.

Given the fact that $\widetilde{\boldsymbol{\lambda}}$ is nonlinear with respect to $\widetilde{\mathbf{x}}_\mathrm{r}$, the system Eq. (38) has to be solved by means of a nonlinear Newton-Raphson iterative solver. Since $\widetilde{\mathbf{x}}_\mathrm{r}$ is unknown and $\widetilde{\boldsymbol{\lambda}}$ directly depends on $\widetilde{\mathbf{x}}_\mathrm{r}$ via Eq. (3), the contact forces multiharmonic vector $\widetilde{\boldsymbol{\lambda}}$ is also considered as an unknown of the problem. The main objective of the DLFT-HBM is to solve the nonlinear constrained optimization problem associated with contact without using Lagrange multipliers, that would double the size of the system.

The DLFT-HBM methodology uses augmented lagrangians $\widetilde{\boldsymbol{\lambda}}$ in order to estimate contact forces and the main unknown of the problem for the solver is $\widetilde{\mathbf{x}}_\mathrm{r}$. In a more practical way, the Newton-Raphson procedure iterates over the displacement field $\widetilde{\mathbf{x}}_\mathrm{r}$, and at the $k$-th iteration, the contact forces $\widetilde{\boldsymbol{\lambda}}^k$ are estimated thanks to the optimization solver iterate $\widetilde{\mathbf{x}}_\mathrm{r}^k$.

The augmented lagrangian methodology relies on a modification of the nonlinear function residual $\mathcal{H}_\mathrm{r}(\widetilde{\mathbf{x}}_\mathrm{r})$ by including a constraint. For DLFT-HBM, since $\widetilde{\mathbf{x}}_\mathrm{r}$ is the unknown used in the optimization process, the incorporated constraint is the gap positivity condition: $\mathbf{g} \geq \mathbf{0}$. Before proceeding, it is necessary to define the gap function in the frequency domain. In the presented case, contact nodes are not necessarily co-located so $g(t) = x_\mathrm{r}(t) + g_0(t)$ where $g_0(t)$ is the distance between the contact nodes of undeformed structures. In the frequency domain, this expression can be written such as,

$$\widetilde{\mathbf{g}}_\mathbf{x} = \widetilde{\mathbf{x}}_\mathrm{r} + \widetilde{\mathbf{g}}_0 \tag{39}$$

where $\widetilde{\mathbf{g}}_0 = \mathcal{F}\left\{g_0(t_i)\right\}_{i=1\ldots N_\mathrm{t}}$ and $\widetilde{\mathbf{g}}_\mathbf{x}$ is the multiharmonic vector of the gap function associated to the displacement field $\mathbf{x}_\mathrm{r}$.

The DLFT-HBM methodology relies on a prediction-correction scheme in order to produce an estimate of the contact forces $\widetilde{\boldsymbol{\lambda}}^k$ and then compute the residual of the objective function Eq. (38) at the $k$-th iteration.

### 2.4.2 Prediction step

As a starting point, the contact forces are predicted in the frequency domain by isolating $\widetilde{\boldsymbol{\lambda}}$ in the equilibrium equation Eq. (38) and including the gap constraint weighted by a positive penalty factor $\varepsilon$:

$$\widetilde{\boldsymbol{\lambda}}_\mathbf{x}^k = \widetilde{\mathbf{f}}_{\mathrm{ex,r}} - \mathbf{Z}_\mathrm{r}\widetilde{\mathbf{x}}_\mathrm{r}^k - \varepsilon\widetilde{\mathbf{g}}_\mathbf{x}^k \tag{40}$$

This expression cannot be used in the frequency domain since UCC apply on the variables $g$ and $\lambda$ in the time domain. Hence, the predicted contact forces are transferred to the time domain by IDFT:

$$\boldsymbol{\lambda}_\mathbf{x}^k = \overline{\mathcal{F}}\widetilde{\boldsymbol{\lambda}}_\mathbf{x}^k \tag{41}$$

where $\boldsymbol{\lambda}_\mathbf{x}^k = \left\{\lambda_\mathbf{x}^k(t_i)\right\}_{i=1\ldots N_\mathrm{t}}$. The introduction of the term $\varepsilon\widetilde{\mathbf{g}}_\mathbf{x}$ has the objective of penalizing the contact forces in order to induce the respect of the gap constraint. Its impact over the contact forces can be detailed into three cases in the time domain, say at time $t_i$:

- **violation of gap constraint** ($g_\mathbf{x}^k(t_i) < 0$): the penalty term increases the equilibrium's residual, ensuring no solution can be found with a large violation of $\mathbf{g} \geq 0$,
- **separation** ($g_\mathbf{x}^k(t_i) > 0$): the penalty term makes the prediction $\lambda_\mathbf{x}^k(t_i)$ negative if $\varepsilon$ is large enough, allowing to detect contact phases based on the sign of $\lambda_\mathbf{x}^k(t_i)$,
- **contact** ($g_\mathbf{x}^k(t_i) \simeq 0$): the penalty term is small and has few influence over the residual.

The negative values of the contact forces violate the contact force positivity condition, however this defect of the predicted forces is adressed in the following correction step.

### 2.4.3 Correction step

In order to compute the actual contact forces $\boldsymbol{\lambda}^k = \left\{\lambda^k(t_i)\right\}_{i=1\dots N_\mathrm{t}}$ from the predicted ones $\boldsymbol{\lambda}^k_\mathbf{x}$, it is needed to make a correction step such as:

$$\lambda^k(t_i) = \lambda^k_\mathbf{x}(t_i) + \lambda^k_\mathbf{y}(t_i) \quad \forall i \in [\![1, N_\mathrm{t}]\!] \tag{42}$$

where $\lambda^k_\mathbf{y}(t_i)$ is the correction of the contact force at time $t_i$. These corrections are computed based on the sign of the predicted contact forces:

- **separation** ($\lambda^k_\mathbf{x}(t_i) < 0$): the contact force should be zero, implying that $\lambda^k(t_i) = 0$ and $\lambda^k_\mathbf{y}(t_i) = -\lambda^k_\mathbf{x}(t_i)$,
- **contact** ($\lambda^k_\mathbf{x}(t_i) > 0$): the contact force is equal to the prediction, so $\lambda^k(t_i) = \lambda^k_\mathbf{x}(t_i)$ and $\lambda^k_\mathbf{y}(t_i) = 0$.

The switching condition between the two states is based on the sign of predicted contact forces. This allows to circumvent the oscillating nature of the gap that oscillates around zero during a contact phase in the HBM framework. The detection is then smoother when considering the sign of the predicted contact forces as it prevents oscillations between contact and separation even if the gap function oscillates around zero.

It is worth noting that the correction step annihilates the negative values of the contact forces generated through the introduction of the penalty term. In the end, the corrections ensure that contact forces $\boldsymbol{\lambda}^k$ respect the positivity condition: $\boldsymbol{\lambda}^k \geq \mathbf{0}$.

Following the correction step, the contact forces multiharmonic vector $\widetilde{\boldsymbol{\lambda}}^k$ is computed by transforming $\boldsymbol{\lambda}^k$ back to the frequency domain through a DFT. $\widetilde{\boldsymbol{\lambda}}^k$ can then be used in order to compute the residual of the objective function Eq. (43), such as:

$$\mathcal{H}_\mathrm{r}(\widetilde{\mathbf{x}}^k_\mathrm{r}) = \mathbf{Z}_\mathrm{r}\widetilde{\mathbf{x}}^k_\mathrm{r} + \widetilde{\boldsymbol{\lambda}}^k(\widetilde{\mathbf{x}}^k_\mathrm{r}) - \widetilde{\mathbf{f}}_{\mathrm{ex,r}} \tag{43}$$

In order to advance in the Newton-Raphson procedure, the computation of a numerical value for the residual is sufficient as it allows to compute the jacobian matrix of the system by finite differences if the latter cannot be formulated as an analytical expression. The optimization solver corrects the iterate until the residual of the objective function is sufficiently close to zero. The DLFT-HBM nested in the optimization procedure is illustrated in Fig. 3, this figure also allows to understand how the different variables are linked with each other.

### 2.4.4 Properties of the solutions

This section aims to showcase a property of the solutions found by DLFT-HBM: the value of the penalty factor $\varepsilon$ does not have a physical influence over the solutions.

The convergence of the methodology is dependent on the penalization of the predicted contact forces, because the latter intervenes in the prediction of the contact forces Eq. (40). However, the way the methodology is built ensures that solutions found by the DLFT-HBM satisfy the equation of motion in the frequency domain and respect the UCC, for any value of $\varepsilon$. This property is guaranteed thanks to the way the corrections $\boldsymbol{\lambda}^k_\mathbf{y} = \left\{\lambda^k_\mathbf{y}(t_i)\right\}_{i=1\dots N_\mathrm{t}}$ are built. Indeed, the corrections $\lambda^k_\mathbf{y}(t_i)$ can only take positive or null values and a strict complementarity is ensured between $\boldsymbol{\lambda}^k_\mathbf{y}$ and $\boldsymbol{\lambda}^k$: $\boldsymbol{\lambda}^k_\mathbf{y} \perp \boldsymbol{\lambda}^k$ (see Sec. 2.4.3). Thanks to these two properties, one may write the following:

$$\mathbf{0} \leq \boldsymbol{\lambda}^k_\mathbf{y} \perp \boldsymbol{\lambda}^k \geq \mathbf{0} \tag{44}$$

Given the relation between the couple of variables $(\boldsymbol{\lambda}^k_\mathbf{y}, \boldsymbol{\lambda}^k)$, it is possible to derive that $\boldsymbol{\lambda}^k_\mathbf{y}$ is proportional to a theoretical gap function that strictly respects the UCC such that $\boldsymbol{\lambda}^k_\mathbf{y} = \varepsilon \mathbf{g}^k_\mathbf{y}$, and it follows,

$$\mathbf{0} \leq \frac{1}{\varepsilon}\boldsymbol{\lambda}^k_\mathbf{y} = \mathbf{g}^k_\mathbf{y} \perp \boldsymbol{\lambda}^k \geq \mathbf{0} \tag{45}$$

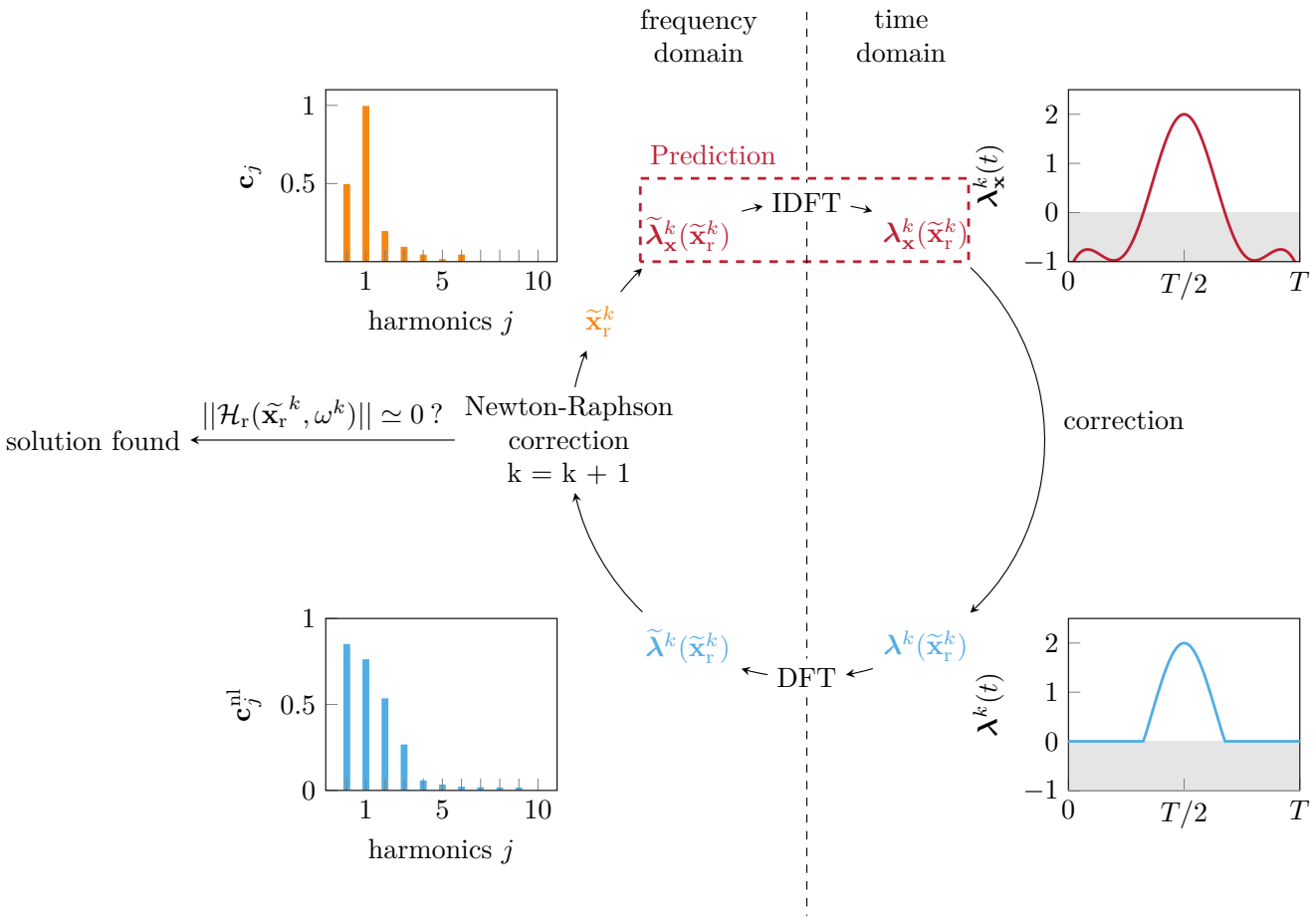


**Figure 3.** DLFT-HBM procedure.

The theoretical variable $\mathbf{g}_{\mathbf{y}}^{k}$ is not explicitly calculated throughout any iteration of the procedure but its definition helps to demonstrate the properties of the procedure. Following the observation of Eq. (45), it is possible to express the corrected nonlinear forces $\widetilde{\boldsymbol{\lambda}}^{k}$ thanks to Eq. (42) as:

$$\widetilde{\boldsymbol{\lambda}}^{k} = \widetilde{\boldsymbol{\lambda}}_{\mathbf{x}}^{k} + \widetilde{\boldsymbol{\lambda}}_{\mathbf{y}}^{k} = \widetilde{\mathbf{f}}_{\mathrm{ex,r}} - \mathbf{Z}_{\mathrm{r}}\widetilde{\mathbf{x}}_{\mathrm{r}}^{k} - \varepsilon(\widetilde{\mathbf{g}}_{\mathbf{x}}^{k} - \widetilde{\mathbf{g}}_{\mathbf{y}}^{k}) \tag{46}$$

Substituting Eq. (46) into the DLFT-HBM objective function Eq. (43) yields:

$$\mathcal{H}_{\mathrm{r}}(\widetilde{\mathbf{x}}_{\mathrm{r}}^{k}) = \mathbf{Z}_{\mathrm{r}}\widetilde{\mathbf{x}}_{\mathrm{r}}^{k} + \underbrace{\widetilde{\mathbf{f}}_{\mathrm{ex,r}} - \mathbf{Z}_{\mathrm{r}}\widetilde{\mathbf{x}}_{\mathrm{r}}^{k} - \varepsilon(\widetilde{\mathbf{g}}_{\mathbf{x}}^{k} - \widetilde{\mathbf{g}}_{\mathbf{y}}^{k})}_{\widetilde{\boldsymbol{\lambda}}^{k}} - \widetilde{\mathbf{f}}_{\mathrm{ex,r}} = -\varepsilon(\widetilde{\mathbf{g}}_{\mathbf{x}}^{k} - \widetilde{\mathbf{g}}_{\mathbf{y}}^{k}) \tag{47}$$

In the end, the convergence criterion of the DLFT-HBM is controlled by the difference between the gap function of the system $\widetilde{\mathbf{g}}_{\mathbf{x}}$ and the theoretical one $\widetilde{\mathbf{g}}_{\mathbf{y}}$ weighted by $\varepsilon$. The alternative expression of the objective function Eq. (47) provides a new interpretation of the residual: $\mathcal{H}_{\mathrm{r}}(\widetilde{\mathbf{x}}_{\mathrm{r}}^{k})$ is a numerical measure of the respect of the UCC by the couple $(\widetilde{\mathbf{g}}_{\mathbf{x}}^{k}, \widetilde{\boldsymbol{\lambda}}^{k})$. Indeed, when the Newton-Raphson iterative procedure finds a solution, the residual of the

objective function is close to zero, so:

$$\left\|\mathcal{H}_{\mathrm{r}}(\widetilde{\mathbf{x}}_{\mathrm{r}}^{k})\right\| \simeq 0 \quad \Rightarrow \quad \widetilde{\mathbf{g}}_{\mathbf{x}}^{k} \simeq \widetilde{\mathbf{g}}_{\mathbf{y}}^{k} \tag{48}$$

Since the couple $(\mathbf{g}_{\mathbf{y}}^{k}, \boldsymbol{\lambda}^{k})$ strictly respects the UCC, it follows from Eq. (48) that $(\mathbf{g}_{\mathbf{x}}^{k}, \boldsymbol{\lambda}^{k})$ also respects the UCC:

$$\mathbf{0} \leq \mathbf{g}_{\mathbf{y}} \simeq \mathbf{g}_{\mathbf{x}} \perp \boldsymbol{\lambda} \geq \mathbf{0} \tag{49}$$

Finally, it is possible to verify that this convergence criterion also ensures that the equation of motion is respected by construction of the contact forces $\widetilde{\boldsymbol{\lambda}}^{k}$ from Eq. (42):

$$\widetilde{\boldsymbol{\lambda}}^{k} = \widetilde{\mathbf{f}}_{\mathrm{ex,r}} - \mathbf{Z}_{\mathrm{r}}\widetilde{\mathbf{x}}_{\mathrm{r}}^{k} - \underbrace{\varepsilon(\widetilde{\mathbf{g}}_{\mathbf{x}}^{k} - \widetilde{\mathbf{g}}_{\mathbf{y}}^{k})}_{\simeq 0} \Rightarrow \mathbf{Z}_{\mathrm{r}}\widetilde{\mathbf{x}}_{\mathrm{r}}^{k} + \widetilde{\boldsymbol{\lambda}}^{k}(\widetilde{\mathbf{x}}_{\mathrm{r}}^{k}) - \widetilde{\mathbf{f}}_{\mathrm{ex,r}} \simeq \mathbf{0} \tag{50}$$

All the conditions are then satisfied and the solution found by the DLFT-HBM is in fact a solution to the vibro-impact problem. Actually, $\varepsilon$ has no influence over the physical nature of the solutions and acts like a numerical tolerance on the UCC.

## 2.5 LCP-HBM

When it comes to the respect of the UCC in structural dynamics, a new approach has emerged in recent years [1, 16, 26, 27, 46]. Numerous methods have been developed in order to tackle the UCC by solving linear complementarity problems (LCP), in time integration schemes [1, 16, 27], or even associated with the HBM [26]. This type of problem belongs to the family of constrained optimization problems, requiring the use of dedicated solvers. Often more costly in terms of computation times, these solvers lead to solutions that strictly respect Eq. (51), unlike methods that involve regularized and/or penalized contact for instance.

$$\begin{cases} \mathbf{g} = \mathbf{W}\boldsymbol{\lambda} + \mathbf{p} & \text{(51a)} \\ 0 \leq \mathbf{g} \perp \boldsymbol{\lambda} \geq 0 & \text{(51b)} \end{cases}$$

The convex analysis concepts involved in the formulation of a LCP are strictly equivalent to those used to formulate a nonsmooth mechanical problem [1], this makes the LCP a theoretical tool particularly well-suited for the solution of contact problems.

In order to formulate a LCP for a structural contact problem, since Eq. (51b) already stands for the UCC, the only step is to derive a linear relation between $\mathbf{g}$ and $\boldsymbol{\lambda}$ of the form of Eq. (51a) from the equation of motion. In the case of HBM, one must derive a relation of the type $\mathbf{g} = \mathbf{W}\boldsymbol{\lambda} + \mathbf{p}$ from the harmonic equation of motion Eq. (23). This relation should be formulated in the time domain for the LCP to be relevant. The association of the HBM with a LCP resolution was initially proposed in [26], the resulting strategy is denominated LCP-HBM. In this article, the LCP-HBM is modified to consider oversampled time signals, contrarily with [26].

### 2.5.1 Constraint matrix

As a first step towards the derivation of the LCP-HBM problem, it is necessary to define the constraint matrix $\mathbf{c}_{\mathrm{N}}^{\top}(t)$. This matrix is directly linked to the contact configuration and the geometry of the problem. It allows to compute the gap function $g(t)$ from the displacement field $\mathbf{x}(t)$ and the nonlinear forces $\mathbf{f}_{\mathrm{nl}}(t)$ knowing the Lagrange multipliers $\lambda(t)$:

$$g(t) = \mathbf{c}_{\mathrm{N}}^{\top}(t)\mathbf{x}(t) + \mathbf{g}_0(t) \tag{52a}$$

$$\mathbf{f}_{\mathrm{nl}}(t) = \lambda(t)\mathbf{c}_{\mathrm{N}}(t) \tag{52b}$$

In order to illustrate the geometrical interpretations of $\mathbf{c}_{\mathrm{N}}^{\top}$, Fig. 4 shows how the local quantities $(\lambda, g)$ are linked to the absolute quantities $(\mathbf{f}_{\mathrm{nl}}, \mathbf{x})$ through the constraint matrix, in a unidimensional configuration.

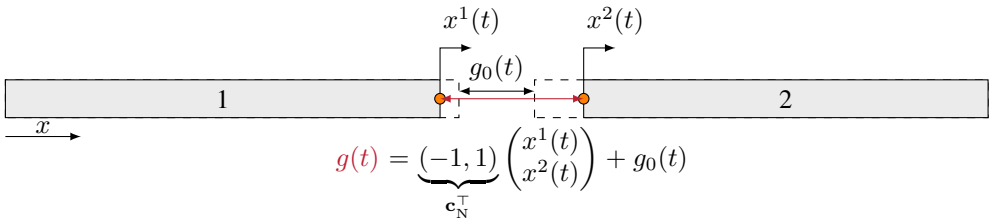


**(a)** Relation between $g$ and $\mathbf{x}$.

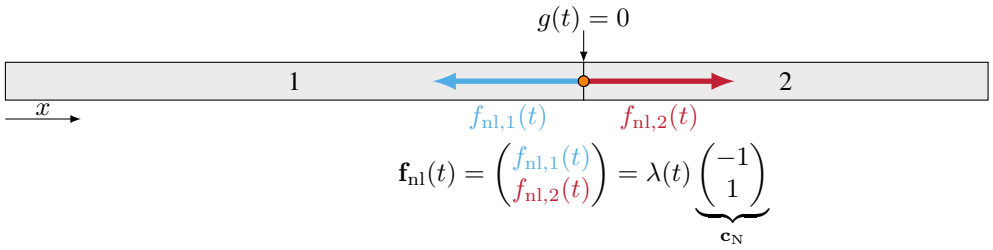


**(b)** Relation between $\lambda$ and $\mathbf{f}_\mathrm{nl}$.

**Figure 4.** Geometrical interpretation of $\mathbf{c}_\mathrm{N}^\top$.

In the configuration presented in Fig. 4, the constraint matrix is $\mathbf{c}_\mathrm{N} = \begin{pmatrix} -1 \\ 1 \end{pmatrix}$. In this particular case, it is not dependent on time because the normal vector to the contact interface is always oriented on the same axis $x$. In three-dimensional applications, this is not always the case and the time dependence of the constraint matrix must then be accounted for.

### 2.5.2 Derivation of the LCP-HBM equation

The present section aims to detail the mathematical developpements necessary to obtain the linear relation between $\mathbf{g}$ and $\boldsymbol{\lambda}$. For these developpements, Eq. (23) is chosen as a starting point before the harmonic condensation steps presented in Sec. 2.2. The developpements are made for a single contact constraint, but this methodology can easily be extended to several contact constraints.

In order to formulate the HBM problem in the time domain, it is necessary – by analogy with the AFT procedure – to define a time discretization covering a period where the calculations are carried out. The time instants of the discretization are noted $t_i$, with $i \in [\![1, N_\mathrm{t}]\!]$. Following this, Eqs. (52a) and (52b) can be cast into systems of $N_\mathrm{t}$ equations on the whole discretization such as:

$$\mathbf{g} = \mathbf{C}_\mathrm{N}^\top \mathbf{X} + \mathbf{g}_0 \tag{53a}$$

$$\mathbf{F}_\mathrm{nl} = \mathbf{C}_\mathrm{N} \boldsymbol{\lambda} \tag{53b}$$

where $\mathbf{g} = \{g(t_i)\}_{i=1\dots N_\mathrm{t}}$ is the discretized gap function, $\mathbf{X} = \{\mathbf{x}(t_i)\}_{i=1\dots N_\mathrm{t}}$ is the discretized displacement field, $\mathbf{g}_0 = \{g_0(t_i)\}_{i=1\dots N_\mathrm{t}}$ is the discretized initial gap, $\mathbf{F}_\mathrm{nl} = \{\mathbf{f}_\mathrm{nl}(t_i)\}_{i=1\dots N_\mathrm{t}}$ is the discretized nonlinear force and $\boldsymbol{\lambda} = \{\lambda(t_i)\}_{i=1\dots N_\mathrm{t}}$ the discretized Lagrange multiplier. In the same manner, the matrix $\mathbf{C}_\mathrm{N}^\top$ contains the constraint matrix $\mathbf{c}_\mathrm{N}(t)$ at each time step:

$$\mathbf{C}_\mathrm{N}^\top = \begin{pmatrix} \mathbf{c}_\mathrm{N}^\top(t_1) & & (\mathbf{0}) \\ & \ddots & \\ (\mathbf{0}) & & \mathbf{c}_\mathrm{N}^\top(t_{N_\mathrm{t}}) \end{pmatrix} \tag{54}$$

The classical HBM equation Eq. (23) involves both unknown multiharmonic vectors $\widetilde{\mathbf{x}}$ and $\widetilde{\mathbf{f}}_\mathrm{nl}(\widetilde{\mathbf{x}})$. In order to derive the linear relation between $\mathbf{g}$ and $\boldsymbol{\lambda}$, it is then necessary to substitute $\widetilde{\mathbf{x}}$ and $\widetilde{\mathbf{f}}_\mathrm{nl}(\widetilde{\mathbf{x}})$ by their time-discretized

counterparts thanks to Eqs. (53a) and (53b). The substitution of the contact forces is quite straight-forward by transferring Eq. (53b) into the frequency domain:

$$\widetilde{\mathbf{f}}_{\mathrm{nl}} = \mathcal{F}\mathbf{F}_{\mathrm{nl}} = \mathcal{F}\mathbf{C}_{\mathrm{N}}\boldsymbol{\lambda} \tag{55}$$

Substituting Eq. (55) into Eq. (23) yields:

$$\mathbf{Z}\widetilde{\mathbf{x}} + \mathcal{F}\mathbf{C}_{\mathrm{N}}\boldsymbol{\lambda} = \widetilde{\mathbf{f}}_{\mathrm{ex}} \tag{56}$$

Once $\boldsymbol{\lambda}$ has been substituted, the next step is to express $\mathbf{g}$ into Eq. (56). In order to do so, a relation between $\mathbf{g}$ and $\widetilde{\mathbf{x}}$ is obtained by substituting $\mathbf{X} = \overline{\mathcal{F}}\widetilde{\mathbf{x}}$ in Eq. (53a):

$$\mathbf{g} = \mathbf{g}_0 + \mathbf{C}_{\mathrm{N}}^{\top}\mathbf{X} = \mathbf{g}_0 + \mathbf{C}_{\mathrm{N}}^{\top}\overline{\mathcal{F}}\widetilde{\mathbf{x}} \tag{57}$$

For the purpose of using Eq. (57) into Eq. (56), it is necessary to multiply Eq. (56) by $\mathbf{C}_{\mathrm{N}}^{\top}\overline{\mathcal{F}}\mathbf{Z}^{-1}$:

$$\mathbf{C}_{\mathrm{N}}^{\top}\overline{\mathcal{F}}\widetilde{\mathbf{x}} + \mathbf{C}_{\mathrm{N}}^{\top}\overline{\mathcal{F}}\mathbf{Z}^{-1}\mathcal{F}\mathbf{C}_{\mathrm{N}}\boldsymbol{\lambda} = \mathbf{C}_{\mathrm{N}}^{\top}\overline{\mathcal{F}}\mathbf{Z}^{-1}\widetilde{\mathbf{f}}_{\mathrm{ex}} \tag{58}$$

Finally, from Eqs. (58) and (57), one may write the following relation:

$$\mathbf{g} - \mathbf{g}_0 + \mathbf{C}_{\mathrm{N}}^{\top}\overline{\mathcal{F}}\mathbf{Z}^{-1}\mathcal{F}\mathbf{C}_{\mathrm{N}}\boldsymbol{\lambda} = \mathbf{C}_{\mathrm{N}}^{\top}\overline{\mathcal{F}}\mathbf{Z}^{-1}\widetilde{\mathbf{f}}_{\mathrm{ex}} \tag{59}$$

At this point, both multiharmonic vectors $\widetilde{\mathbf{x}}$ and $\widetilde{\mathbf{f}}_{\mathrm{nl}}$ were substituted with the time-discretized variables $\mathbf{g}$ and $\boldsymbol{\lambda}$: Eq. (59) has become a linear relation between $\boldsymbol{\lambda}$ and $\mathbf{g}$ of the following form:

$$\mathbf{g} = \mathbf{W}\boldsymbol{\lambda} + \mathbf{p} \tag{60}$$

where $\mathbf{W}$ and $\mathbf{p}$ can be identified as follows:

$$\mathbf{W} = -\mathbf{C}_{\mathrm{N}}^{\top}\overline{\mathcal{F}}\mathbf{Z}^{-1}\mathcal{F}\mathbf{C}_{\mathrm{N}} \tag{61a}$$

$$\mathbf{p} = \mathbf{C}_{\mathrm{N}}^{\top}\overline{\mathcal{F}}\mathbf{Z}^{-1}\widetilde{\mathbf{f}}_{\mathrm{ex}} + \mathbf{g}_0 \tag{61b}$$

Knowing $\mathbf{W}$ and $\mathbf{p}$, the LCP-HBM problem is completely defined. It is possible to provide a LCP solver with the couple ($\mathbf{W}$, $\mathbf{p}$) in order to search for a solution to the following LCP-HBM problem:

$$\begin{cases} \mathbf{g} = \underbrace{\left(-\mathbf{C}_{\mathrm{N}}^{\top}\overline{\mathcal{F}}\mathbf{Z}^{-1}\mathcal{F}\mathbf{C}_{\mathrm{N}}\right)}_{\mathbf{W}}\boldsymbol{\lambda} + \underbrace{\mathbf{C}_{\mathrm{N}}^{\top}\overline{\mathcal{F}}\mathbf{Z}^{-1}\widetilde{\mathbf{f}}_{\mathrm{ex}} + \mathbf{g}_0}_{\mathbf{p}} & \text{(62a)} \\ 0 \leq \mathbf{g} \perp \boldsymbol{\lambda} \geq 0 & \text{(62b)} \end{cases}$$

Once the problem Eq. (62) is solved, the couple of variables ($\mathbf{g}$, $\boldsymbol{\lambda}$) is known on the whole period as an output. In the HBM framework, in order to retrieve the associated solution displacement field $\widetilde{\mathbf{x}}$, it is necessary to linearly solve the HBM system using the previously determined contact forces $\boldsymbol{\lambda}$ as known external forces:

$$\mathbf{Z}\widetilde{\mathbf{x}} = \widetilde{\mathbf{f}}_{\mathrm{ex}} - \mathcal{F}\mathbf{C}_{\mathrm{N}}\boldsymbol{\lambda} \tag{63}$$

In the same manner as the AFT procedure, the oversampling of contact forces generates harmonic contributions beyond the HBM bandwidth. These harmonics are filtered away when substituting $\boldsymbol{\lambda}$ in the HBM equation. In fact, the LCP-HBM method can be qualified as a pseudo-AFT strategy since there is a need to solve the system Eq. (62) on time-discretized unknowns $\boldsymbol{\lambda}$ and $\mathbf{g}$ as a first step and then linearly solve the frequential system Eq. (63) with known contact forces $\boldsymbol{\lambda}$. The whole strategy is summed up in Fig. 5.

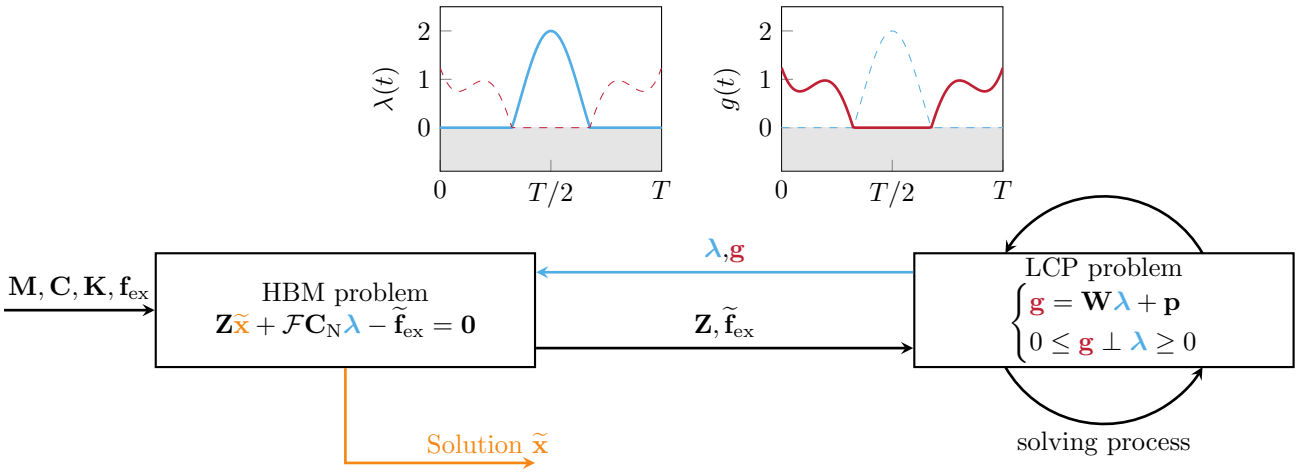


**Figure 5.** LCP-HBM procedure.

### 2.5.3 Solution methods for a LCP

Since the LCP is a class of problems involving a system of equations under inequalities and complementarity conditions, a dedicated LCP solving method must be employed. Such algorithms are generally divided into two categories, that are pivoting algorithms and iterative algorithms:

- **iterative algorithms** [10] are Newton-like iterative algorithms that take into account the supplementary constraints of the LCP problems.
- **pivoting methods** [1, 24] take advantage of the algebraic nature of the system by swapping and sorting the different columns and rows of $\mathbf{W}$ and $\mathbf{p}$.

For this paper, the Lemke pivoting algorithm is chosen since it was successfully used in the case of rubbing interactions involving an industrial finite elements model [26]. For algorithmic reasons, pivoting methods are restricted to the computation of solutions when the problem does not have trivial solutions *i.e.* $\boldsymbol{\lambda} = \mathbf{0}$. As a consequence, this defect prevents the computation of full nonlinear frequency response curves (NFRC) in the presence of turning points. Turning points are generally responsible for the coexistence of trivial and non-trivial solutions at the same pulsation. However, this flaw does not prevent to make qualitative comparisons of the LCP-HBM with other methods presented in this work.

The LCP-HBM methodology developped in this article uses rectangular Fourier matrices so that the time domain is oversampled in order to gain in precision. This point correponds to the main difference with the strategy developped in [26] where Fourier matrices are kept square. However, the oversampling empirically leads to the singularity of $\mathbf{W}$, which can be attributed to the loss of information in the oversampled Fourier transforms. Though, the singularity of $\mathbf{W}$ does not affect the convergence of the Lemke's algorithm.

## 3 Assessement of harmonic methods

The objective of this section is to assess DLFT-HBM and LCP-HBM through of an academic rod model. The model and the strategy is firstly presented and followed by a presentation of the different characteristics of the solutions found by the different harmonic methodologies through various types of obstacle. Finally, a presentation of NFRC is made to account for the robustness of the continuation procedure.

### 3.1 Models & strategy

In order to assess the DLFT-HBM and LCP-HBM methodologies, a finite element unidimensional rod model impacting a flexible obstacle is considered [6], it is represented in Fig. 6. The obstacle is considered to be a single

spring of stiffness $k_{\text{obs}}$. It has been introduced in order to make the simulations of a gradual difficulty. Such phenomenological models are usually used to evaluate numerical strategies for contact [6, 26, 45]. An harmonic

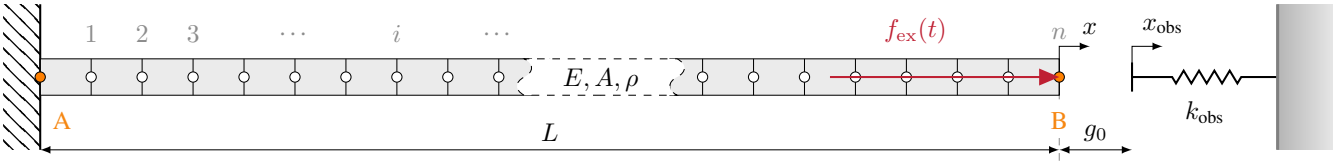


**Figure 6.** Model with a flexible obstacle (adapted from [6]).

excitation force $f_{\text{ex}}(t)$ of angular pulsation $\omega$ is applied on the contact node. The gap function associated with the contact constraint is $g(t) = x_{\text{obs}}(t) - x(t)$. The elementary mass and stiffness matrices of a rod in traction and compression are given by:

$$\mathbf{M}_{\text{e}} = \frac{\rho A l}{6}\begin{bmatrix} 2 & 1 \\ 1 & 2 \end{bmatrix} \text{ and } \mathbf{K}_{\text{e}} = \frac{EA}{l}\begin{bmatrix} 1 & -1 \\ -1 & 1 \end{bmatrix} \tag{64}$$

with $E$ the Young modulus, $l$ the beam length, $\rho$ the density and $A$ the section area, whose values are given in Tab. 1.

| $A$ | $E$ | $\rho$ | $L$ | $g_0$ | $n$ |
|---|---|---|---|---|---|
| $15.6\,\text{cm}^2$ | 210 GPa | $7800\,\text{kg}\cdot\text{m}^{-3}$ | 13 cm | 0.2 mm | 20 |

**Table 1.** Rod model parameters.

The final objective is to be able to characterize contact interactions with a rigid obstacle. To this end, the obstacle stiffness is increased in order to approach the rigid obstacle behaviour. The values of stiffness for $k_{\text{obs}}$ range from $1 \cdot 10^9\,\text{N}\cdot\text{m}^{-1}$ to $1 \cdot 10^{11}\,\text{N}\cdot\text{m}^{-1}$. As a reference, the equivalent stiffness of the rod is about $k_{\text{rod}} = 2.5 \cdot 10^9\,\text{N}\cdot\text{m}^{-1}$, it is the result of a ratio between a unitary force applied at the end of the rod over the static displacement generated by this force. In order to put the stiffness of the obstacle into perspective with the rod's flexibility, $k_{\text{obs}}$ is normalized with respect to $k_{\text{rod}}$: $k_{\text{obs}}$ ranges from $0.4k_{\text{rod}}$ to $40k_{\text{rod}}$. The range of stiffness for the obstacle was chosen so that the obstacle goes from weakly nonlinear when $k_{\text{obs}} = 0.4k_{\text{rod}}$, to highly nonlinear when $k_{\text{obs}} = 40k_{\text{rod}}$. For instance, in the configuration where $k_{\text{obs}} = 40k_{\text{rod}}$, the obstacle is so stiff that it is hardly displaced at all. In the paper, the flexible obstacle configuration refers to the configuration represented in Fig. 6, regardless of the value of $k_{\text{obs}}$. To the contrary, the rigid obstacle configuration refers to the configuration represented in Fig. 7 where the obstacle is perfectly rigid and no contact stiffness is involved in the simulations. This last configuration is numerically very

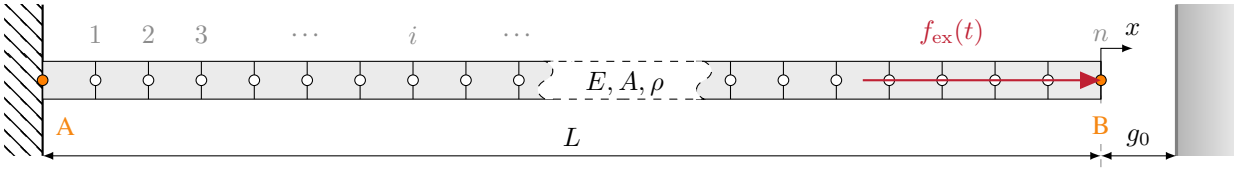


**Figure 7.** Model with a rigid obstacle (adapted from [6]).

challenging since the DLFT-HBM method was mainly used and tested on configurations where both structures are flexible. The excitation amplitude is chosen to be $f_{\text{ex}} = 25 \cdot 10^3\,\text{N}$, this corresponds to a linear vibration amplitude of $\|x(t)\|_\infty = 5.36 \cdot 10^{-4}\,\text{m}$ at the first eigenfrequency $\omega_0 = 63\,953\,\text{rad}\cdot\text{s}^{-1}$. The linear frequency response curve is given

in Fig. 8. The rod model's cutoff frequency is around $\omega_{\max} = 2.81 \cdot 10^6\,\mathrm{rad{\cdot}s^{-1}} \simeq 44\omega_0$ for both the clamped-free and free-free configurations.

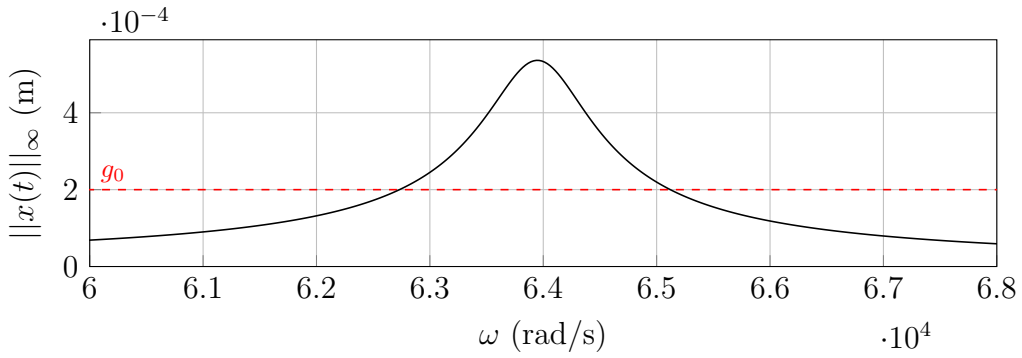


**Figure 8.** Linear forced response curve, vibration amplitude of the contact node (—), intial gap $g_0$ (- -).

### 3.2 Reference solutions: time integration

The reference solution provided in this paper is based on an explicit Time Integration (TI) procedure [4]. By construction of the integration scheme, the strict respect of the UCC is ensured. The time step is taken as $\mathrm{d}t = 10^{-7}$s in order to have numerical stability of the integration scheme. The reference solution at $\omega = \omega_0$ is represented in Fig. 9.

Both solutions respect the UCC, but the Fig. 9b displays a displacement of the obstacle related to its stiffness that is, by definition, not present for the rigid obstacle. The type of obstacle obviously affects the dynamics of the rod. In fact, this affects mainly the spectrum of the contact forces. The rigid obstacle generates more high frequency content, such as an impulsional sollicitation numerically traducing a strong velocity discontinuity. Thanks to the flexibility of the obstacle, the contact forces appear to be filtered. This will have a particular importance for harmonic resolutions. The influence of the flexibility of the obstacle on the contact forces spectrum is represented in Fig. 10a. This representation shows the benefits of using a flexible obstacle: it acts like low-pass filter for the contact forces that are generally broadband. For most of $k_{\mathrm{obs}}$ values, the forces are converged around the Lagrange spectrum (—) until approximately $44\omega_{\mathrm{res}}$ (corresponds to the cutoff frequency of the model) (- -), after which signals begin to differ. This shows that it can be almost impossible to capture the very high frequency participations caused by nonsmooth phenomena such as velocity discontinuities. The main limitation of the HBM being its finite bandwidth, a non negligible part of the contact forces spectrum has to be filtered out. However, as observed in Fig. 10b, the mechanical structure also acts like a low-pass filter because the displacement spectrum is not as broad as the contact forces spectrum.

### 3.3 Flexible obstacle

In this section, thorough examinations are made on LCP-HBM and DLFT-HBM solutions on a single point at $\omega = \omega_0$ for $k_{\mathrm{obs}} = 4k_{\mathrm{rod}}$. Both solutions are converged in terms of displacement field as represented in Fig. 11. The solutions appear identical in terms of absolute displacement in Fig. 11a but the contact laws simulated by both HBM methods are slightly different as shown in Fig. 11b after substracting the reference TI signal to the solutions. In fact, according to Fig. 11b, the small differences at the contact phase around $T/2$ induce larger differences in the free-flight phase. The behaviours of the different solutions are represented in the contact phase on a zoomed view in Fig. 11c.

In order to evaluate the simulated contact laws, it is necessary to investigate the quantities $\mathbf{g}$ and $\boldsymbol{\lambda}$ represented in Fig. 12, for both HBM strategies the contact forces are represented in the time domain before the filtering induced by the DFT $\mathcal{F}$ that neglects harmonics generated through oversampling. For the LCP-HBM, the time-discretized $\boldsymbol{\lambda}$ is displayed straight out of the Lemke's algorithm, before truncature. For the DLFT-HBM, $\boldsymbol{\lambda}$ is retrieved from the

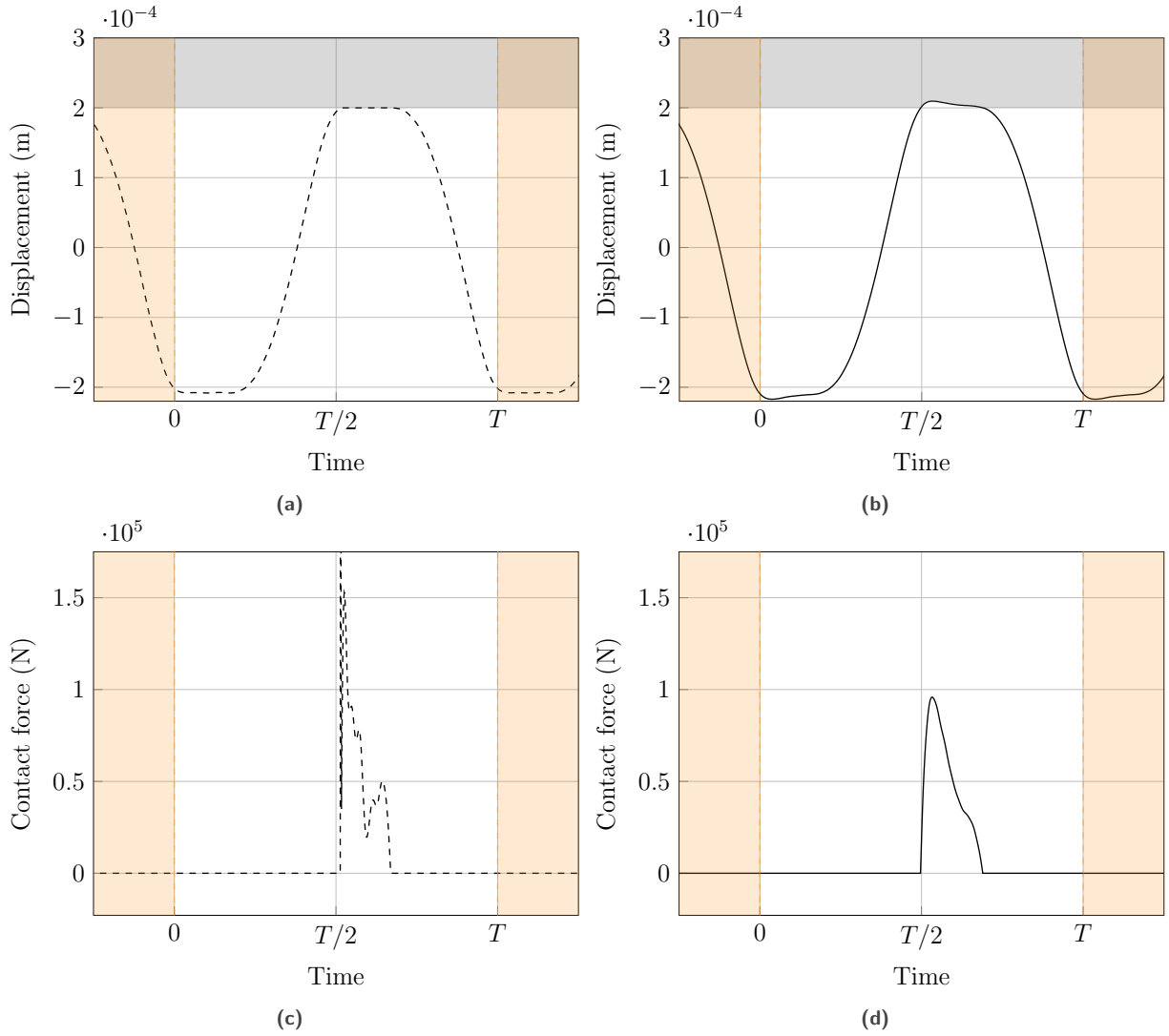


**Figure 9.** Reference solutions for the two configurations (a) displacements with a rigid obstacle , (b) displacements with a flexible obstacle, (c) contact forces with a rigid obstacle , (d) contact forces with a flexible obstacle, TI rigid obstacle (**- -** ), TI flexible obstacle with $k_{\text{obs}} = 4k_{\text{rod}}$ (**—**), obstacle ( ).

time domain in the AFT procedure at the last iteration right before applying the DFT. Since the contact forces are oversampled in the time domain ($N_{\text{t}} \gg 2N_{\text{h}} + 1$), the spectral contributions are still broadband because of nonsmoothness of the contact law. However, these signals do not represent the actual forces injected in the system since the frequency content beyond $N_{\text{h}}\omega$ is not considered in the HBM system resolution.

The gap signals show two ways of handling contact. In fact, the DLFT-HBM's gap in Fig. 12b appears to oscillate around $g = 0$ and becomes negative whereas the LCP-HBM gap in Fig. 12a strictly respects the $\mathbf{g} \geq \mathbf{0}$ condition. On the other hand, contact forces before filtering are also of different nature. Indeed, the DLFT-HBM force signal in Fig. 12d is superimposed with the TI reference in the time domain but the LCP-HBM contact forces in Fig. 12c are of impulsional nature and appear to be non-physical. This is actually because the solution to a LCP problem intrinsically respects the complementarity conditions and in this case, the UCC are strictly respected before filtering. However, since these signals are inscribed in the HBM framework, these results need to be truncated to the HBM bandwidth in order to be physically analyzed. These truncated contact forces are represented in Fig. 13.

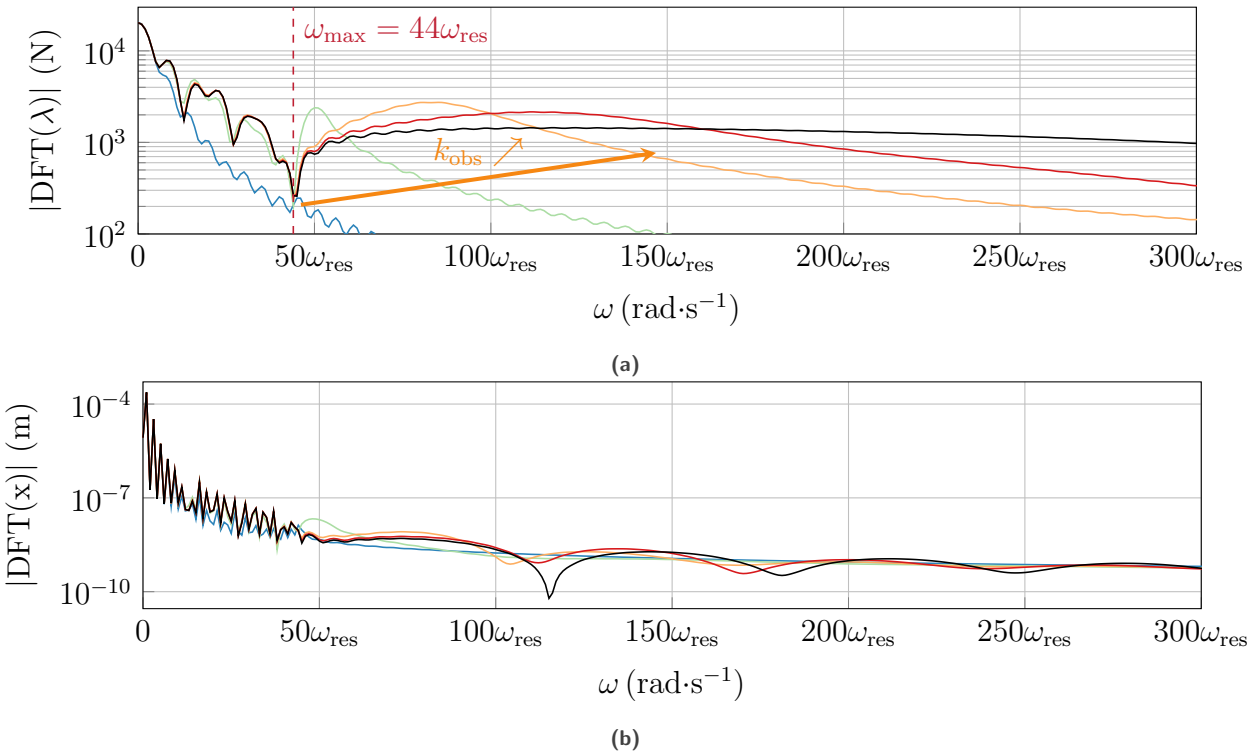


**Figure 10.** Spectrum for TI simulations with variable $k_{obs}$ at $\omega_{res} = \omega_0$, (a) contact forces, (b) displacements, Lagrange (—), $k_{obs} = 4k_{rod}$ (—), $k_{obs} = 40k_{rod}$ (—), $k_{obs} = 200k_{rod}$ (—), $k_{obs} = 400k_{rod}$ (—).

For both strategies, the truncated contact forces are computed by making a back and forth transformation in the frequency domain on the time-discretized contact forces $\boldsymbol{\lambda}$ represented on Fig. 12.

The filtering of the nonsmooth contact forces lead in both cases to truncature oscillations. The truncated signals are the actual contact forces that the system undergo. This shows that both methods fail to respect the $\boldsymbol{\lambda} \geq \mathbf{0}$ condition. The oscillations also invalidate the $\boldsymbol{\lambda}^\top \mathbf{g} = 0$ condition since contact forces are not zero as the gap is still positive. The observations made on the gap and truncated contact forces can be summed up in Fig. 14.

The unilateral contact curve (—) represents the portion of the $(g, \lambda)$ space on which all UCC are respected. The HBM simulated contact laws represented in Fig. 14 approximate the reference unilateral law. The conclusions remain the same: DLFT-HBM allow residual penetration where LCP-HBM does not and both methods generate truncature oscillations on contact forces.

### 3.4 Rigid obstacle with penalty

The results shown in Sec. 3.3 have presented a number of properties on HBM methods when the obstacle can be modeled by a single stiffness, which is not the general case. In this part, the perspective is changed in order to analyze further the methodologies. The obstacle is no longer considered flexible, but rigid with a bilinear penalty law. The flexible obstacle presented in Sec. 3.3 and the rigid obstacle with a bilinear penalty law are strictly equivalent. The only difference between these two configurations is a post-processing consideration. Indeed, in the rigid with penalty case the gap differs and becomes:

$$g(t) = g_0 - x(t) \tag{65}$$

This means that was previously considered as the displacement of the obstacle is now considered as residual

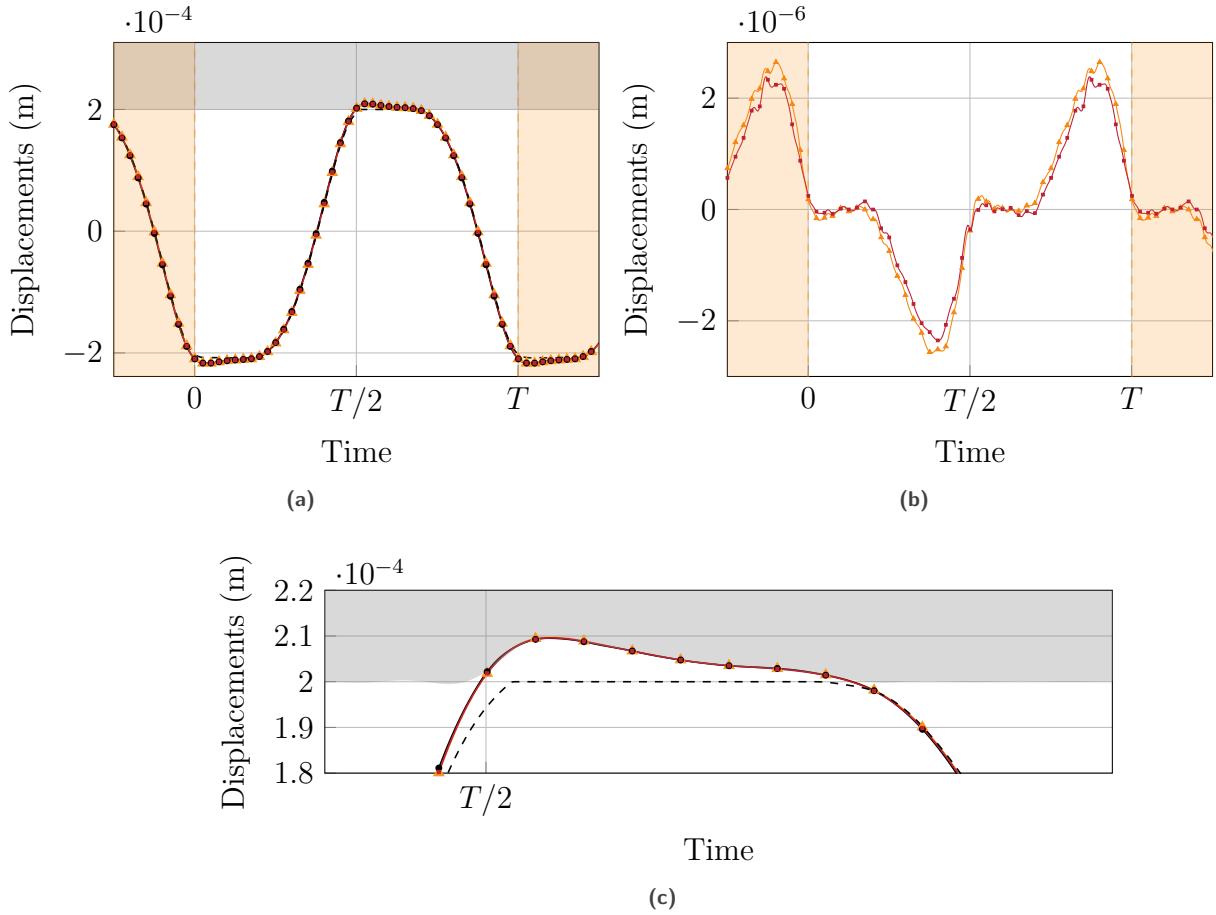


**Figure 11.** Displacement of the contact node for $N_\mathrm{h} = 20$ and $N_\mathrm{t} = 400$, (a) absolute displacements, (b) deviation from the TI reference (only DLFT-HBM and LCP-HBM), (c) absolute displacements around the contact area, TI (flexible obstacle) (—●—), TI (rigid obstacle) (- - ), DLFT-HBM (—▲—), LCP-HBM (—●—), obstacle (▭).

penetration: a defect of the contact treatment. The dynamics of the rod is the exactly the same, however the contact law diagrams are different due to the new expression of the gap function $g(t)$. It is possible to display the HBM simulated contact laws for several values of $k_\mathrm{obs}$ in Fig. 15.

The $k_\mathrm{obs}$ stiffness influences the residual penetration since it is directly related to the asymptotic contact law $\lambda = \max(-k_\mathrm{obs} g, 0)$. Within this framework, the HBM methods tend towards the $k_\mathrm{obs}$ bilinear penalty law. If the penalty stiffness is sufficiently large, this allows to approximate a rigid obstacle. As expected from the equivalence with the flexible obstacle simulations, the DLFT-HBM and LCP-HBM behave in the same manner as in Sec. 3.3. Indeed, LCP-HBM solutions do not penetrate in the sense of penalty and respect the following inequality $\boldsymbol{\lambda} \geq \max(-k_\mathrm{obs}\mathbf{g}, \mathbf{0})$. The DLFT-HBM solution oscillates around the asymptotic law and its behaviour is quite the same as in Sec. 3.3. This change of perspective only allows to visually see the influence of the penalty stiffness on the residual penetration, which was not possible when the obstacle's displacement was not considered as a defect of the methodology (*i.e* flexible obstacle).

### 3.5 Rigid obstacle

Finally, it is also possible to directly consider the obstacle as completely rigid without using a penalty stiffness, it refers to the model represented in Fig. 7. The solutions given for this model are converged in amplitude for every

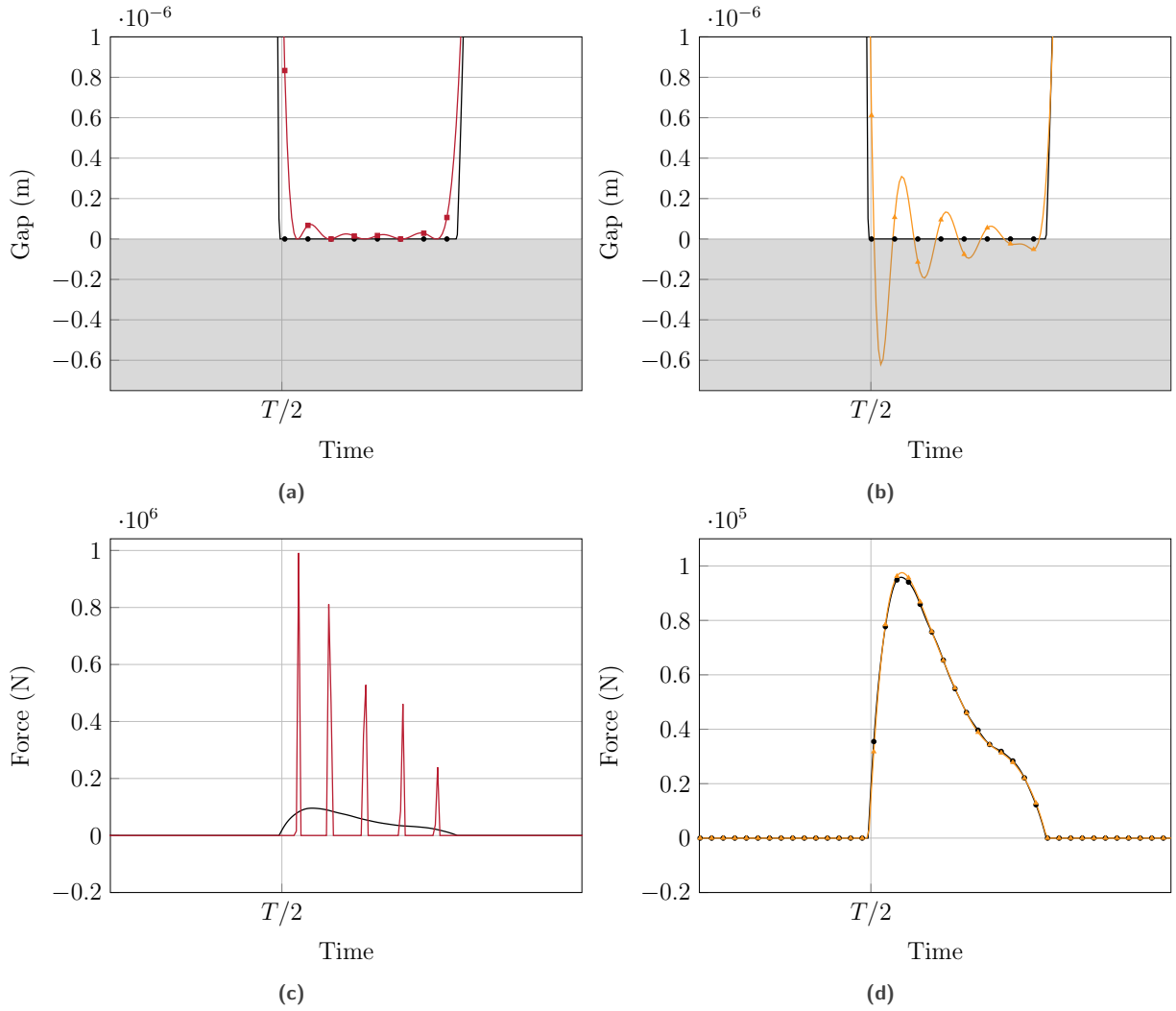


**Figure 12.** Gap and contact forces prior to DFT filtering for a flexible obstacle for $N_\mathrm{h} = 20$ and $N_\mathrm{t} = 400$, (a) LCP-HBM gap, (b) DLFT-HBM gap, (c) LCP-HBM contact forces pre-filtering, (d) DLFT-HBM contact forces pre-filtering, TI flexible obstacle (—●—), DLFT-HBM (—▲—), LCP-HBM (—■—), obstacle (▭).

value of $\varepsilon$ that allows the solver to find a solution. This is important as it underlines the relevance of the solution in terms of amplitude without any study on the $\varepsilon$ convergence. In terms of behaviour, there are no significant differences with the results presented in Sec. 3.3: it shows a robustness of the strategy with respect to the type of obstacle.

### 3.6 Nonlinear frequency response curves

It is possible to obtain NFRC by coupling the DLFT-HBM with an arc-length continuation procedure [42] as well as a bordering algorithm [19] to ensure convergence at points of singular jacobian matrix. The equation of motion is normalized in time and space as a step of numerical preconditioning for the continuation procedure. These calculations are done for the flexible obstacle case and the stiffness of the obstacle ranges from $k_\mathrm{obs} = 0.4k_\mathrm{rod}$ to $k_\mathrm{obs} = 40k_\mathrm{rod}$ and displayed in Fig. 17. The reference frequency responses are obtained through a TI simulation with a linear chirp excitation on the frequency range of interest for both a rigid obstacle (- - ) and a flexible obstacle

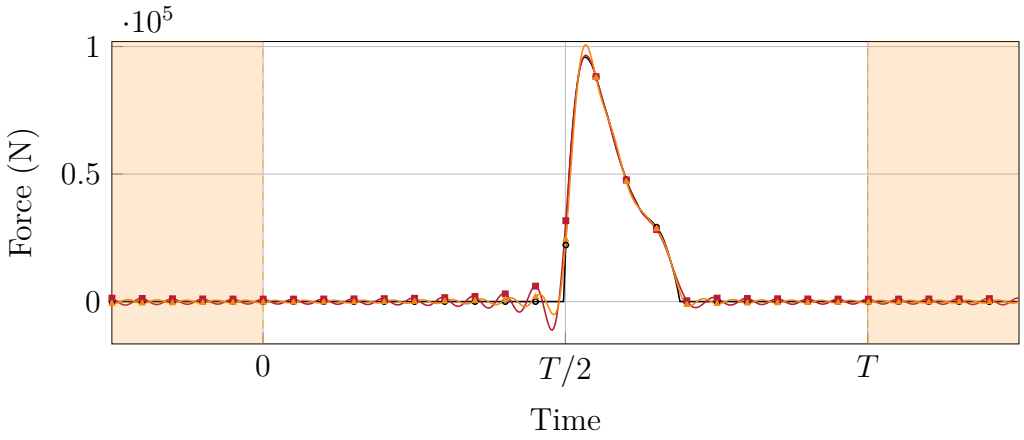


**Figure 13.** Filtered contact forces for a flexible obstacle for $N_\mathrm{h} = 20$ and $N_\mathrm{t} = 400$, TI flexible obstacle (—●—), DLFT-HBM (—▲—), LCP-HBM (—■—).

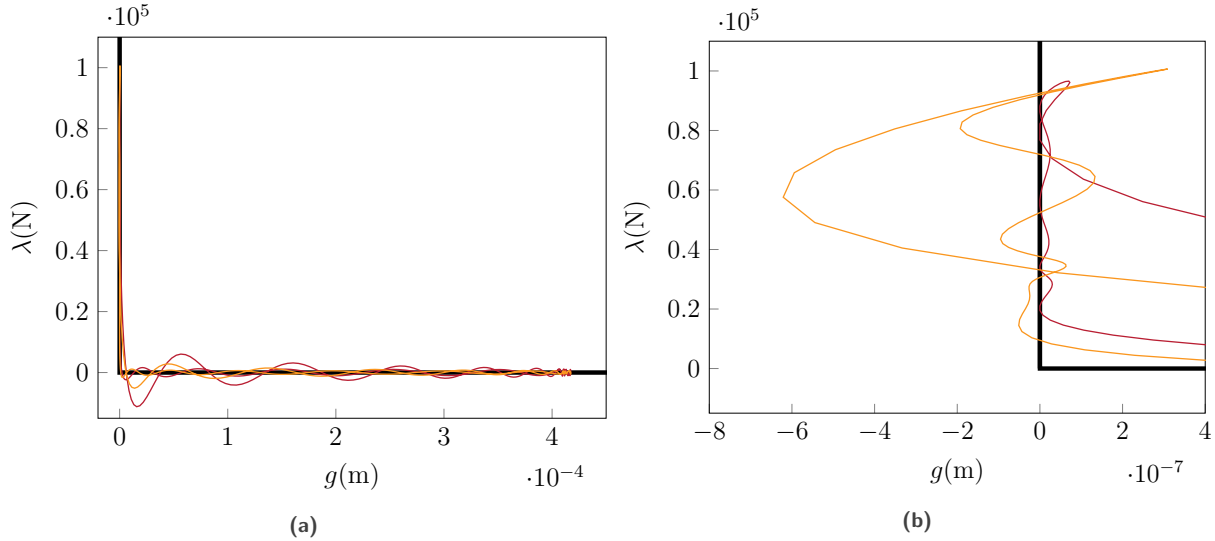


**Figure 14.** Simulated contact laws for $N_\mathrm{h} = 20$ and $N_\mathrm{t} = 400$, (a) whole period, (b) around $g = 0$, DLFT-HBM (—), LCP-HBM (—), unilateral contact (—).

(- -). The chirp excitation formula is given by:

$$\mathbf{f}_\mathrm{ex}(t) = a^1_\mathrm{ex} \cos\left(\left(\omega_1 + (\omega_2 - \omega_1)\frac{t}{2T}\right) t\right) \tag{66}$$

where $a^1_\mathrm{ex}$ is the amplitude of the excitation, $\omega_1$ the instantaneous pulsation of the excitation at $t = 0$, $\omega_2$ the instantaneous pulsation of the excitation at $t = T$ and $T$ the duration of the signal. The LCP-HBM (●), flexible obstacle chirp solutions (- -) and DLFT-HBM (—). The TI chirp simulations experience transient oscillations around the jump from the nonlinear stable branch to the linear branch (around $\omega = 6.6 \cdot 10^4\,\mathrm{rad{\cdot}s^{-1}}$ for the rigid obstacle TI simulation (- -)), this phenomenon is dependent on the sweep rate $(\omega_2 - \omega_1)/2T$ of the chirp simulations. The results shown in Fig. 17 show that LCP-HBM and DLFT-HBM are in good agreement with the reference TI simulations. Moreover, the NFRC show good convergence towards the Lagrange multipliers solutions that confirms

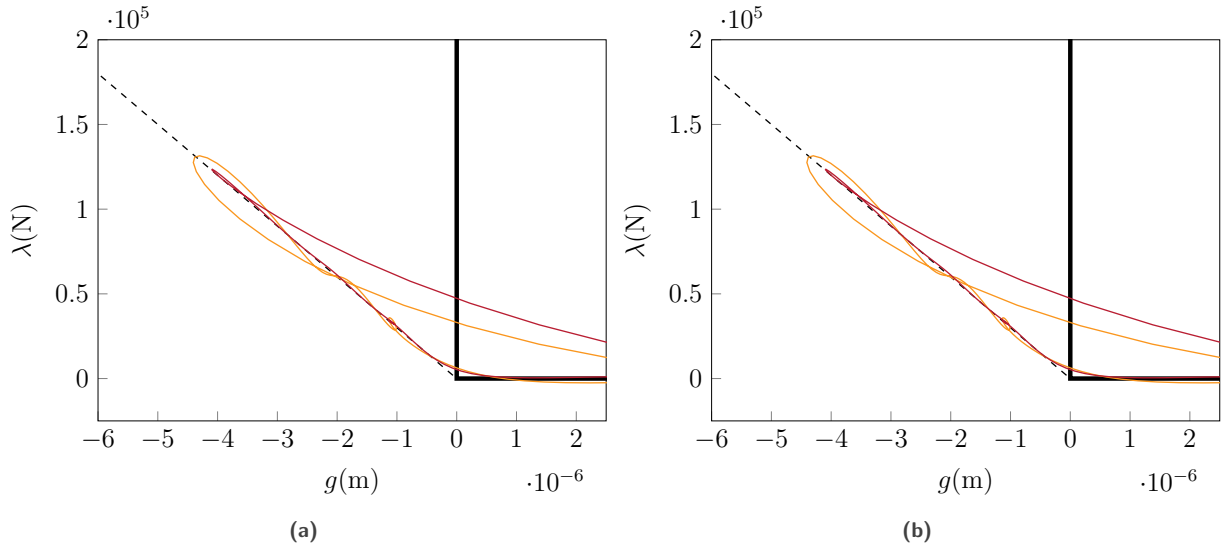


**Figure 15.** Simulated contact laws with variable $k_{\text{obs}}$ around $g = 0$ for $N_{\text{h}} = 20$ and $N_{\text{t}} = 400$, (a) $k_{\text{obs}} = 12k_{\text{rod}}$, (b) $k_{\text{obs}} = 120k_{\text{rod}}$, DLFT-HBM (—), LCP-HBM (—), $\lambda = \max(-k_{\text{obs}}g, 0)$ penalty law (- - ), unilateral contact (▬).

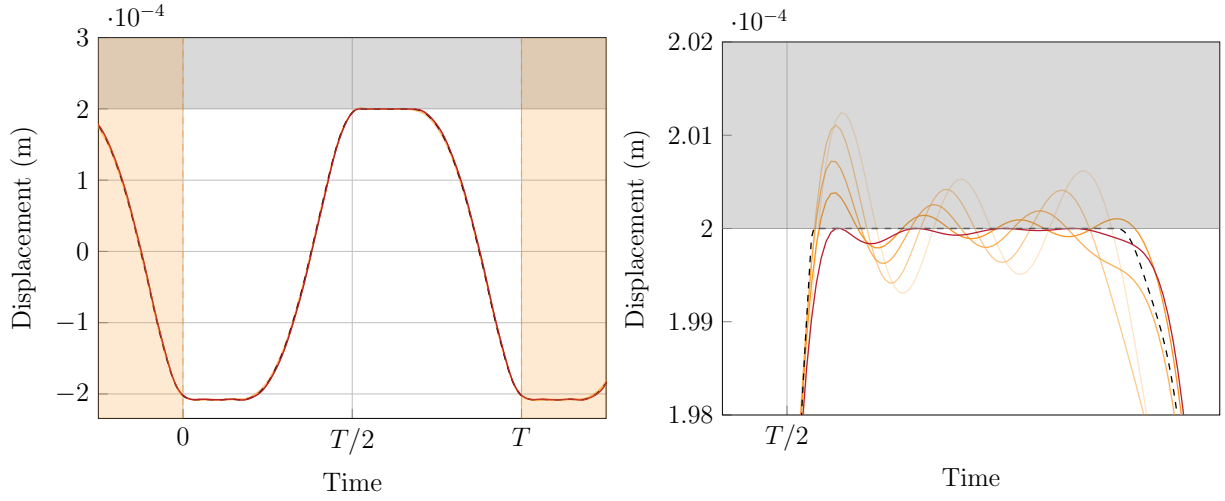


**(a)** Whole period.

**(b)** Contact phase.

**Figure 16.** Displacement of the contact node as a function of $\varepsilon$ for $N_{\text{h}} = 20$ and $N_{\text{t}} = 400$, (a) whole period, (b) contact phase, TI (Lagrange) (- - ), DLFT-HBM $\varepsilon = 1 \cdot 10^8\,\text{N·m}^{-1}$ (—), DLFT-HBM $\varepsilon = 1 \cdot 10^9\,\text{N·m}^{-1}$ (—), DLFT-HBM $\varepsilon = 1 \cdot 10^{10}\,\text{N·m}^{-1}$ (—), DLFT-HBM $\varepsilon = 1 \cdot 10^{11}\,\text{N·m}^{-1}$ (—), LCP-HBM (—), rigid obstacle (▬).

that penalty methods can approximate the dynamics of the rigid obstacle configuration, as shown in [6]. However, significant difficulties are experienced around the turning points in the continuation procedure. Indeed, in order to compute the presented NFRC, the analytical jacobian matrix calculation was necessary in order to converge, its expression is given in A.

It is also possible to obtain DLFT-HBM NRFC for the rigid obstacle configuration. In Fig. 18 NFRC are displayed for both flexible obstacle (- - ) and rigid obstacle (—). The reference solution is the TI solution for a chirp excitation (- - ). A good agreement is shown between the rigid obstacle NRFC and the TI reference. Whereas, the flexible obstacle, equivalent to a penalty method, does not show so good agreement in terms of maximum amplitude. The rigid obstacle simulations have similar computation times as the flexible obstacle. Thus, it is more reliable

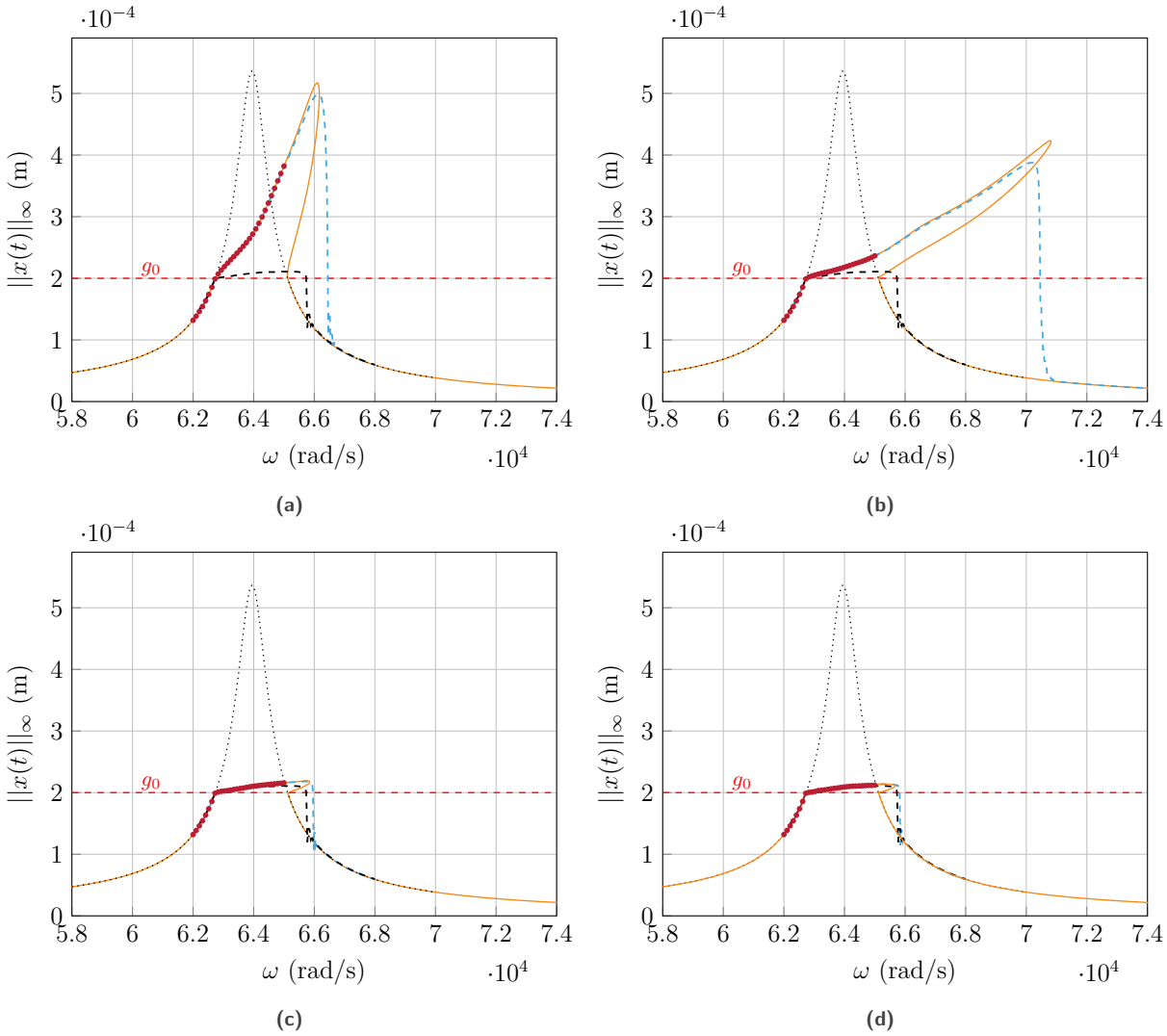


**Figure 17.** NFRC for different values of $k_{\text{obs}}$ for $N_{\text{h}} = 20$ and $N_{\text{t}} = 400$, (a) $k_{\text{obs}} = 0.4k_{\text{rod}}$, (b) $k_{\text{obs}} = 4k_{\text{rod}}$,(c) $k_{\text{obs}} = 20k_{\text{rod}}$ (d) $k_{\text{obs}} = 40k_{\text{rod}}$, linear (····), $g_0$ (- -), TI chirp excitation (rigid obstacle) (- -), DLFT-HBM (—), LCP-HBM (●), TI chirp excitation (flexible obstacle) (- -).

to directly solve the rigid obstacle configuration since they do not require a calibration of $k_{\text{obs}}$ prior to the NFRC calculation.

## 4 Discussion

In order to understand more finely the dependence between the numerical parameters and the quality of the solutions, a parametric study is led on both $\varepsilon$ the DLFT-HBM weighting parameter, and the number of harmonics $N_{\text{h}}$ controlling the length of the Fourier series. These studies aim to highlight the importance of the numerical value of both these parameters. In fact, these parameters play a central role in the complex methodologies presented in this paper, thus it is important to precisely observe their influence over the results to ensure that the solutions found are physically coherent. A spectral analysis is also conducted in order to evaluate the influence of the oversampling of the time signals inside AFT schemes.

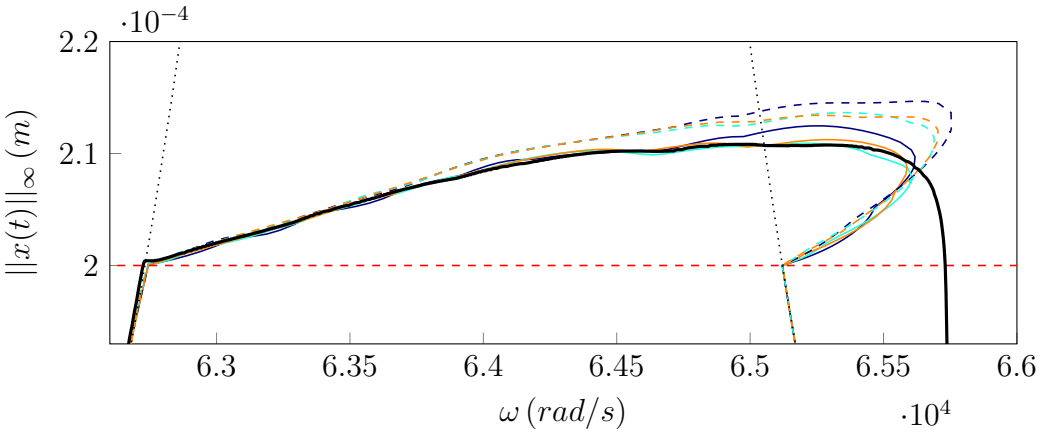


**Figure 18.** NRFC for rigid and flexible obstacle with variable $N_\mathrm{h}$ for $N_\mathrm{t} = 400$, linear (····), $g_0$ (- - ), TI chirp excitation (rigid obstacle) (▬), DLFT-HBM flexible obstacle (- - ), DLFT-HBM rigid obstacle (—), $N_\mathrm{h} = 20$ (▬), $N_\mathrm{h} = 30$ (▬), $N_\mathrm{h} = 40$ (▬).

### 4.1 Influence of $\varepsilon$

The $\varepsilon$ DLFT-HBM parameter is central as it is a numerical quantity that measures how close $\widetilde{\mathbf{g}}_\mathbf{x}$ and $\widetilde{\mathbf{g}}_\mathbf{y}$ have to be for the solution to be considered converged, as stated in Eq. (47). In a way this parameter is analogous to the solver tolerance, which defines how close to zero the residual has to be before convergence. It also has an influence over the DLFT-HBM prediction step at each iteration Eq. (40). Therefore it is interesting to evaluate its influence over the solutions, and in particular on contact forces since it appears in their expression. The contact forces signals are given in Fig. 19 both before and after truncature for several $\varepsilon$ values. The simulations are presented for a flexible obstacle, but the results remain valid for rigid obstacle as well.

The LCP-HBM contact forces are given as a point of comparison. In Fig. 19a, DLFT-HBM contact forces seem to converge towards an impulsional signal as $\varepsilon$ increases. Moreover, the local maxima of the high $\varepsilon$ contact forces seem to coincide with LCP-HBM impulsions. This observation suggest that there is a correlation between both methodologies and that the DLFT-HBM converges towards a solution that strictly respects the UCC in the time domain, like the LCP-HBM. This appears to be counter intuitive since the high $\varepsilon$ solutions do not seem to tend towards the TI signal in the time domain even though they simulate a perfect unilateral contact. However, even if these signals diverge from the TI reference in the time domain before truncature, the truncature cuts all the high frequency contributions generated by the nonsmooth corrections inside the oversampled AFT procedure. The truncated signals represented in Fig. 19b appear to be more coherent with TI during the contact phase, but once again the DLFT-HBM appears to tend towards LCP-HBM and not TI, especially when it comes to truncature oscillations. The amplitude of these oscillations also increases as $\varepsilon$ becomes larger and the LCP-HBM oscillations appear like a maximum bound of the truncature oscillations, this was particularly observed in [26]. The corresponding simulated contact laws diagrams are represented in Fig. 20.

The observations made in Fig. 19 seem to be confirmed in Fig. 20, but this diagram also reveals a more deeper aspect to the $\varepsilon$ convergence: the respect of the $\mathbf{g} \geq \mathbf{0}$ and $\boldsymbol{\lambda} \geq \mathbf{0}$ evolve in opposite directions. As $\varepsilon$ increases, the residual penetration of DLFT-HBM solutions decreases but the truncature oscillations have a greater amplitude. Given how $\varepsilon$ influences the solution, it raises a question towards the choice of its value. Two strategies might be used: taking $\varepsilon$ to the largest possible value leads to a quasi-strict respect of the $\mathbf{g} \geq \mathbf{0}$ condition while there will be large truncature oscillations and thus a poor respect of $\boldsymbol{\lambda} \geq \mathbf{0}$ or chosing $\varepsilon$ as a compromise of both $\mathbf{g} \geq \mathbf{0}$ and $\boldsymbol{\lambda} \geq \mathbf{0}$ conditions.

In order to verify the assumption that the DLFT-HBM tends towards LCP-HBM, it is possible to use a refinement strategy for the value of $\varepsilon$. This methodology consists in calling the DLFT-HBM solver successively with an increasing value of $\varepsilon$ such as $\varepsilon_i = 2\varepsilon_{i-1}$ at the $i^{\text{th}}$ iteration. The essential step to make this strategy work is to provide the

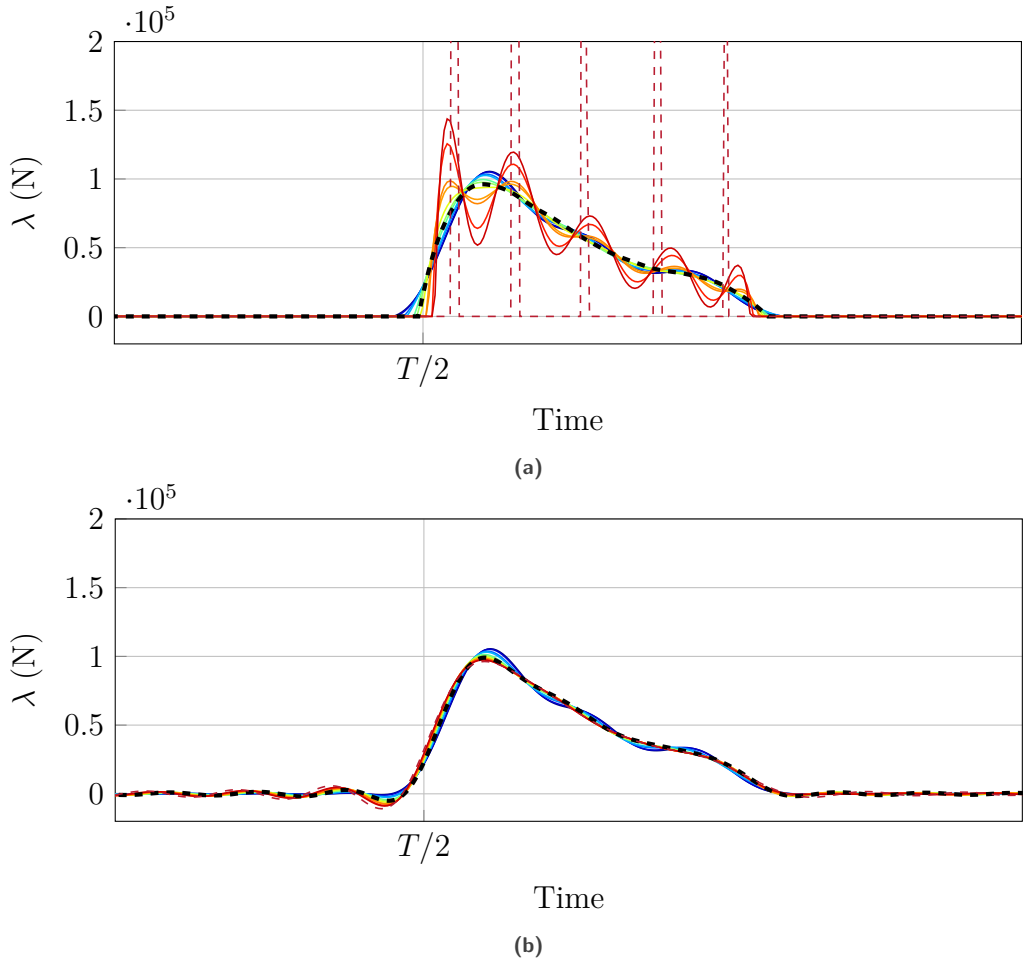


**Figure 19.** Parametric study on $\varepsilon$ for $N_\mathrm{h} = 20$, $N_\mathrm{t} = 600$, $k_\mathrm{obs} = 4k_\mathrm{rod}$ at $\omega = \omega_0$, (a) contact forces before truncature, (b) contact forces after truncature, TI flexible obstacle (- - ), LCP-HBM (- - ), DLFT-HBM (—).

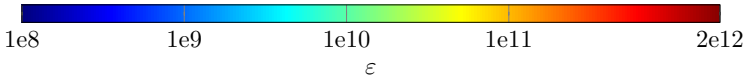


solution of the $(i-1)^{\text{th}}$ iteration as a starting point of the $i^{\text{th}}$ iteration. The solution of the previous iteration being relatively close of the solution of the current iteration, it is a guess that allows the optimization solver to converge on very large values of $\varepsilon$ where a direct resolution would fail. These simulations are conducted on the rigid obstacle case in order to ensure this behaviour on the most challenging model and the results are displayed in Fig. 21.

By refining $\varepsilon$ from $\varepsilon_0 = 1 \cdot 10^{11}\,\mathrm{N{\cdot}m^{-1}}$ to $\varepsilon_{15} = 2^{15}\varepsilon_0 \simeq 1 \cdot 10^{16}\,\mathrm{N{\cdot}m^{-1}}$, the DLFT-HBM simulated contact law appears identical to the one simulated by LCP-HBM. Numerically, having $\varepsilon$ this large means that $\mathbf{g_x}$ and $\mathbf{g_y}$ have become so close that the couple $(\boldsymbol{\lambda}, \mathbf{g_x})$ strictly respects the UCC in the time domain before truncature as does $(\boldsymbol{\lambda}, \mathbf{g_y})$ by construction. DLFT-HBM and LCP-HBM solutions are then equivalent because the latter is built so that the respect of the UCC in the time domain is ensured. This means that both methods, that can be qualified as AFT and pseudo-AFT, present the same defect: the truncature of the contact forces comes with a difficulty to represent the unilateral contact law. The LCP-HBM contact law, which is DLFT-HBM's asymptotic contact law, can be considered as the one lagrangian contact law for the couple $(N_\mathrm{t}, N_\mathrm{h})$ that strictly respects the gap condition

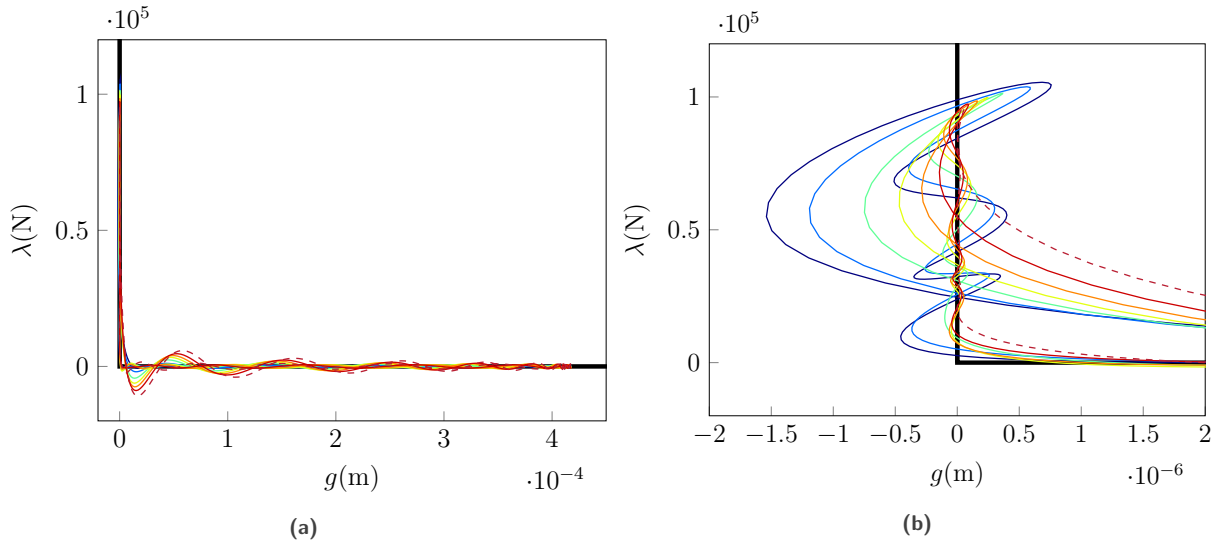


**Figure 20.** Parametric study on $\varepsilon$ for $N_\mathrm{h} = 20$, $N_\mathrm{t} = 600$ at $\omega = \omega_0$: contact laws for $k_\mathrm{obs} = 4k_\mathrm{rod}$ (a) whole period, (b) contact phase (around $g = 0$), LCP-HBM (- -), DLFT-HBM (—), unilateral contact (▬).

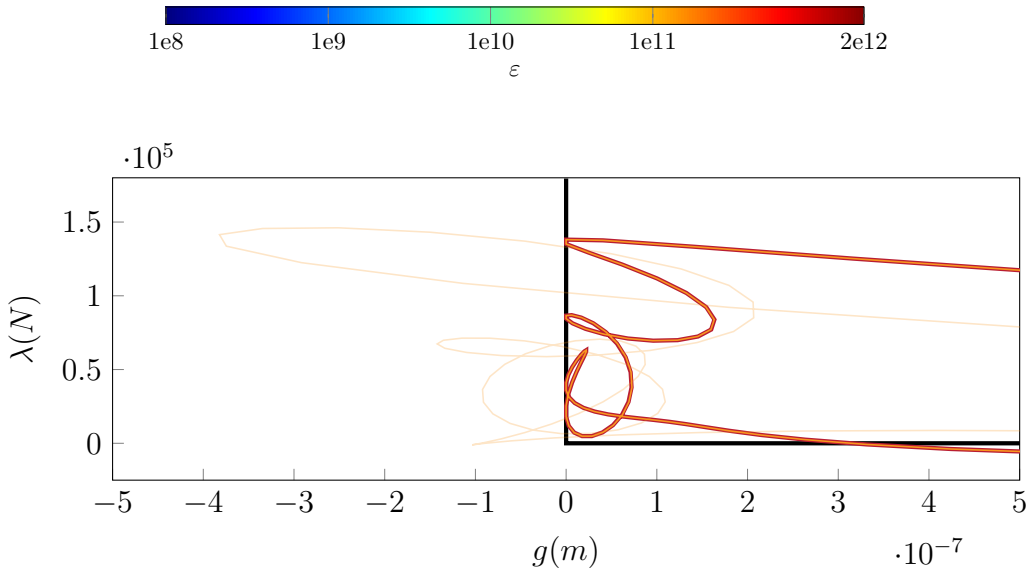


**Figure 21.** Refinement procedure for $\varepsilon$, $N_\mathrm{h} = 20$ and $N_\mathrm{t} = 600$, DLFT-HBM starting point $\varepsilon = \varepsilon_0 = 1 \cdot 10^{11}\,\mathrm{N{\cdot}m^{-1}}$ (—), DLFT-HBM after refinement $\varepsilon = 2^{15}\varepsilon_0 \simeq 1 \cdot 10^{16}\,\mathrm{N{\cdot}m^{-1}}$ (—), LCP-HBM (▬), unilateral contact (▬).

after truncature. It seems that the only improvement that can be done is by widening the bandwidth of resolution (increasing $N_\mathrm{h}$) in order to reduce the influence of the truncature on the contact law, hence describing more precisely the transition from the separated state to the contact state (nonsmoothness). The observation made on Fig. 21 also show that both DLFT-HBM and LCP-HBM do not treat the gap condition and the contact force condition at the same rank: only one of the two is chosen to be respected even after truncature. Indeed, the contact forces still experience spurious oscillations that violate contact conditons even for extremely large values of $\varepsilon$.

### 4.2 Spectral analysis

In order to further investigate the bias of interpreting the pre-filtering contact forces signals inside an AFT procedure, already evoked in Sec. 4.1, it is interesting to represent the spectrum of contact forces for different $\varepsilon$ values represented in Fig. 22.

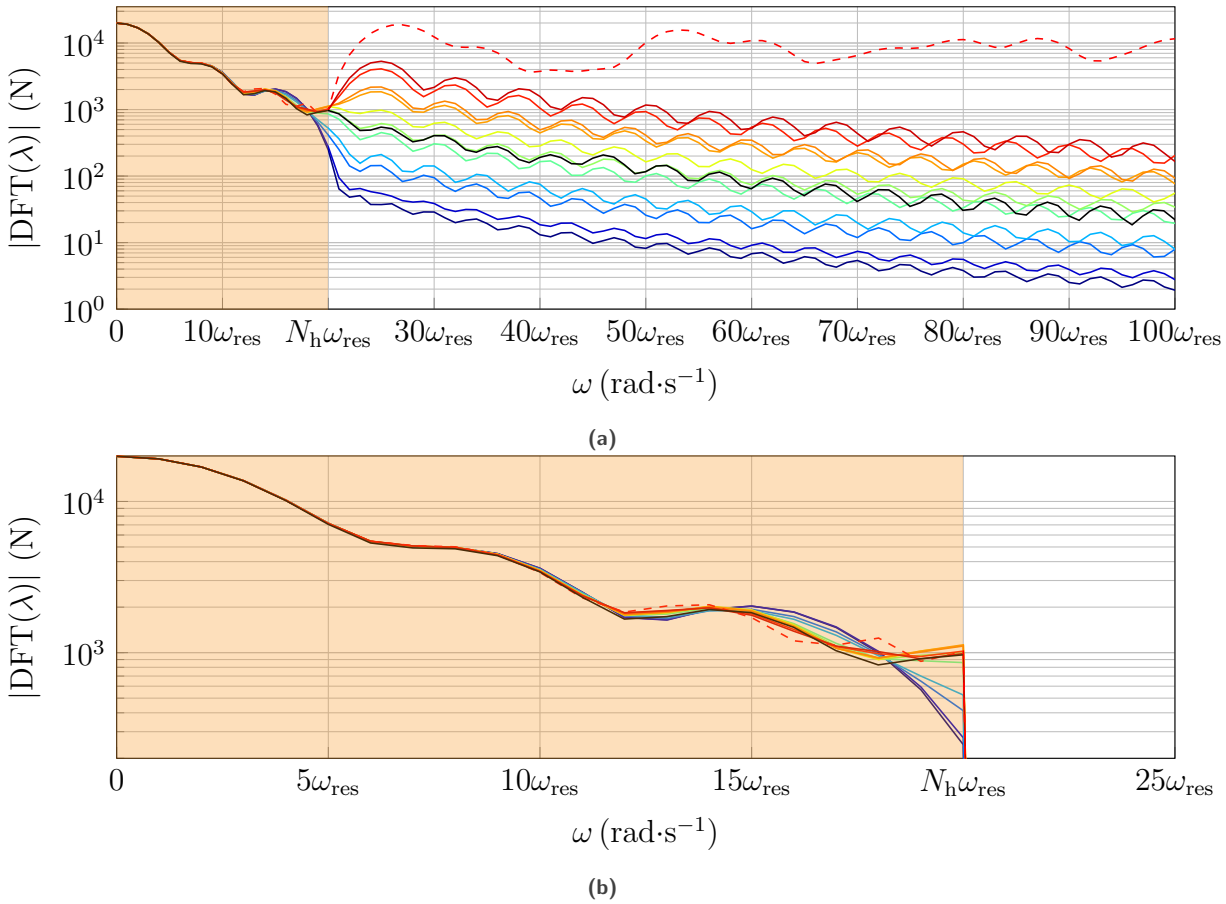


**Figure 22.** Parametric study on $\varepsilon$ for $N_{\mathrm{h}} = 20$ and $N_{\mathrm{t}} = 600$ at $\omega = \omega_0$: contact forces spectrum for $k_{\mathrm{obs}} = 4k_{\mathrm{rod}}$, (a) before truncature, (b) after truncature, TI flexible obstacle (—), LCP-HBM (- -), DLFT-HBM (—), HBM bandwidth ( ).

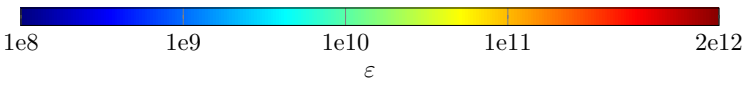


It is possible to compute spectra further than the HBM bandwidth since both methods need to oversample the time domain to fully describe the contact phase. The DLFT-HBM spectra displayed in Fig. 22a show a good concordance with TI inside the HBM bandwidth but the signals do not correlate beyond the cutting frequency. Moreover, according to the value of $\varepsilon$ for DLFT-HBM forces the spectra show a high level of variation. This consolidates the idea that it is not careful to make any physical interpretations on the contact forces prior to truncature and that it is necessary to use the filtered signal before doing so. As displayed in Fig. 22b, the value of $\varepsilon$ has an impact over the spectra inside the HBM bandwidth, but its influence is very limited to the neighbourhood of the asymptotic solution that is the LCP-HBM.

### 4.3 Convergence analysis $N_\mathrm{h}$

The contact laws studied in Sec. 4.1 seem to be limited by the HBM cutting frequency. The influence of the number of harmonics $N_\mathrm{h}$ is assessed in Fig. 23. Increasing this value leads to a decrease of the amplitude of truncature oscillations, moreover the oscillations around $g = 0$ are tightening. This means that all three UCC are positively impacted by an increase of $N_\mathrm{h}$. Obviously, this improvement comes with computational cost and a high level of precision on the contact law is not a necessary condition in order to converge on the system's dynamic response. A number of harmonics around 20 already ensures good nonlinear response curve convergence for the presented rod model application as shown in Sec. 3.6.

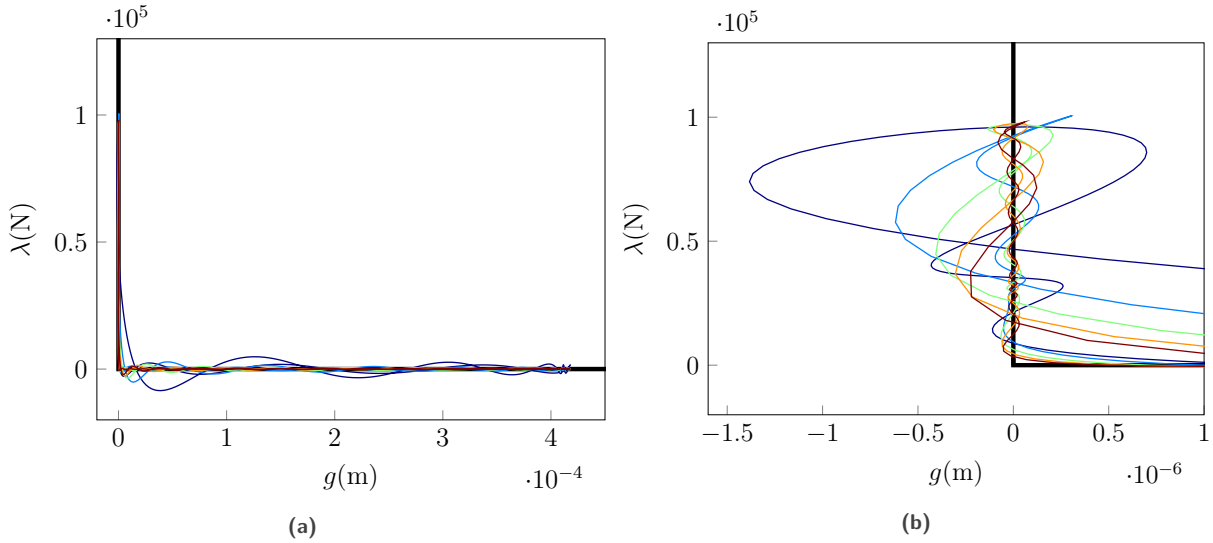


**Figure 23.** Simulated contact law as a function of $N_\mathrm{h}$ for DLFT-HBM with $N_\mathrm{t} = 400$ at $\omega = \omega_0$, (a) whole period, (b) around $g = 0$, $N_\mathrm{h} = 10$ (—), $N_\mathrm{h} = 20$ (—), $N_\mathrm{h} = 30$ (—), $N_\mathrm{h} = 40$ (—), $N_\mathrm{h} = 50$ (—), unilateral contact (—).

## 5 Conclusion

This article presented two Harmonic Balance Method-based numerical strategies using Lagrange multipliers for vibro-impact systems subject to unilateral contact constraints. Both these methodologies provide information over the limits of the AFT procedure as well as the use of lagrangian in frequency formulations. The use of a monodimensionnal rod model reveals the inherent difficulties to such nonsmooth systems. The system is being firstly treated with a flexible obstacle that helps smoothen the contact interactions and acts like a low-pass filter for the contact forces thus restraining the spectral width of the response. The linear complementarity problem taking into account the unilateral contact constraints as part of the resolution, the positive gap condition is ensured on the time signals even after HBM truncature. The dynamic lagrangian formulation appears to restitute a different contact law because the unilateral contact constraints appear in a weaker form in its equations. Introducing a rigid obstacle leads to the validation of the methodology on even more numerically challenging test cases, moreover the nonlinear frequency response curves demonstrate the robustness of the given methodologies. An extensive study over the DLFT-HBM's main numerical parameter shows an asymptotic relation between the two presented strategies: the DLFT-HBM's simulated contact laws asymptotically tend towards the ones given by the LCP-HBM formulation. This observation is attributed to the AFT or pseudo-AFT feature of both strategies as well as a lagrangian formulation on the contact forces, thus favoring the gap condition over the force condition in the unilateral contact constraints. The oversampling of time signals in AFT procedures was investigated and it was shown that non-physical high harmonics are generated that need to be filtered before any interpretation. A final parametric study is led on the number of harmonics and shows that the wider the bandwidth is, the better unilateral contact constraints are respected. This work demonstrates some new aspects in lagrangian contact formulations associated

with the harmonic balance method. Indeed, this paper shows that the LCP-HBM formulation is able to quantitatively describe the contact interactions in an academic case, unlike what was initially proposed in the LCP-HBM founding article [26]. Moreover, the DLFT-HBM numerical parameter $\varepsilon$ has been extensively studied in order to give insights on the choice of its numerical value as well as its influence over the contact laws. Further works will be conducted on the presented methodologies on industrial test cases in the field of turbomachinery to deal with rotor/casing contact interactions.

## Acknowledgments

This research was supported by the Canada Research Chairs Program.

## References

[1] V. Acary and B. Brogliato. Numerical methods for nonsmooth dynamical systems: applications in mechanics and electronics. Lecture notes in applied and computational mechanics 35. Berlin, 2008.

[2] R. Alcorta, S. Baguet, B. Prabel, P. Piteau, and G. Jacquet-Richardet. Period doubling bifurcation analysis and isolated sub-harmonic resonances in an oscillator with asymmetric clearances. Nonlinear Dyn. Vol. 98, No. 4 (2019), 2939–2960. DOI: 10.1007/s11071-019-05245-6. oai : hal-02295420.

[3] T. M. Cameron and J. H. Griffin. An Alternating Frequency/Time Domain Method for Calculating the Steady-State Response of Nonlinear Dynamic Systems. J. Appl. Mech. Vol. 56, No. 1 (1989), 149–154. DOI: 10.1115/1.3176036. oai : hal-01333697.

[4] N. J. Carpenter, R. L. Taylor, and M. G. Katona. Lagrange constraints for transient finite element surface contact. Int. J. Numer. Meth. Engng. Vol. 32, No. 1 (1991), 103–128. DOI: 10.1002/nme.1620320107. oai : hal-01389918.

[5] D. Charleux, C. Gibert, F. Thouverez, and J. Dupeux. Numerical and Experimental Study of Friction Damping Blade Attachments of Rotating Bladed Disks. Int. J. Rotating Mach. Vol. 2006 (2006), 1–13. DOI: 10.1155/IJRM/2006/71302.

[6] Y. Colaïtis and A. Batailly. The harmonic balance method with arc-length continuation in blade-tip/casing contact problems. J. Sound Vib. Vol. 502 (2021), 116070. DOI: 10.1016/j.jsv.2021.116070. oai : hal-03163560.

[7] N. Coudeyras, S. Nacivet, and J.-J. Sinou. Periodic and quasi-periodic solutions for multi-instabilities involved in brake squeal. J. Sound Vib. Vol. 328, No. 4-5 (2009), 520–540. DOI: 10.1016/j.jsv.2009.08.017. oai : hal-00425156.

[8] T. Detroux, L. Renson, L. Masset, and G. Kerschen. The harmonic balance method for bifurcation analysis of large-scale nonlinear mechanical systems. Comput. Methods Appl. Mech. Eng. Vol. 296 (2015), 18–38. DOI: 10.1016/j.cma.2015.07.017. oai : hal-03446374.

[9] C. Duan, T. E. Rook, and R. Singh. Sub-harmonic resonance in a nearly pre-loaded mechanical oscillator. Nonlinear Dyn. Vol. 50, No. 3 (2007), 639–650. DOI: 10.1007/s11071-006-9185-y.

[10] A. Fischer. A Newton-type method for positive-semidefinite linear complementarity problems. J. Optim. Theory Appl. Vol. 86, No. 3 (1995), 585–608. DOI: 10.1007/BF02192160.

[11] F. Fontanela, A. Vizzaccaro, J. Auvray, B. Niedergesäß, A. Grolet, L. Salles, and N. Hoffmann. Nonlinear vibration localisation in a symmetric system of two coupled beams. Nonlinear Dyn. Vol. 103, No. 4 (2021), 3417–3428. DOI: 10.1007/s11071-020-05760-x.

[12] R. J. Gilmore and M. B. Steer. Nonlinear circuit analysis using the method of harmonic balance—A review of the art. Part I. Introductory concepts. Int. J. Microw. Mill.-Wave Comput.-Aided Eng. Vol. 1, No. 1 (1991), 22–37. DOI: 10.1002/mmce.4570010104.

[13] A. Grolet and F. Thouverez. Computing multiple periodic solutions of nonlinear vibration problems using the harmonic balance method and Groebner bases. Mech. Syst. Sig. Process. Vol. 52-53 (2015), 529–547. DOI: 10.1016/j.ymssp.2014.07.015. oai : hal-02121532.

[14] A. Grolet and F. Thouverez. On a new harmonic selection technique for harmonic balance method. Mech. Syst. Sig. Process. Vol. 30 (2012), 43–60. DOI: 10.1016/j.ymssp.2012.01.024. oai : hal-02121478.

[15] T. Heinze, L. Panning-von Scheidt, and J. Wallaschek. Global detection of detached periodic solution branches of friction-damped mechanical systems. Nonlinear Dyn. Vol. 99, No. 3 (2020), 1841–1870. DOI: 10.1007/s11071-019-05425-4.

[16] M. Jean. The non-smooth contact dynamics method. Comput. Methods Appl. Mech. Eng. Vol. 177, No. 3-4 (1999), 235–257. DOI: 10.1016/S0045-7825(98)00383-1. oai : hal-01390459.

[17] S. Jones and M. Legrand. Forced vibrations of a turbine blade undergoing regularized unilateral contact conditions through the wavelet balance method. Int. J. Numer. Meth. Engng Vol. 101, No. 5 (2015), 351–374. DOI: 10.1002/nme.4807. oai : hal-00806545.

[18] S. Karkar, B. Cochelin, and C. Vergez. A high-order, purely frequency based harmonic balance formulation for continuation of periodic solutions: The case of non-polynomial nonlinearities. J. Sound Vib. Vol. 332, No. 4 (2013), 968–977. DOI: 10.1016/j.jsv.2012.09.033. oai : hal-00758184.

[19] H. B. Keller. The Bordering Algorithm and Path Following Near Singular Points of Higher Nullity. SIAM J. Sci. and Stat. Comput. Vol. 4, No. 4 (1983), 573–582. DOI: 10.1137/0904039.

[20] T. Kim, T. Rook, and R. Singh. Super- and sub-harmonic response calculations for a torsional system with clearance nonlinearity using the harmonic balance method. J. Sound Vib. Vol. 281, No. 3-5 (2005), 965–993. DOI: 10.1016/j.jsv.2004.02.039.

[21] W.-J. Kim and N. Perkins. Harmonic balance/Galerkin method for non-smooth dynamic systems. J. Sound Vib. Vol. 261, No. 2 (2003), 213–224. DOI: 10.1016/S0022-460X(02)00949-5.

[22] M. Krack and J. Gross. Harmonic Balance for Nonlinear Vibration Problems. Mathematical Engineering. Cham, 2019. DOI: 10.1007/978-3-030-14023-6.

[23] M. Krack, L. Panning-von Scheidt, and J. Wallaschek. A high-order harmonic balance method for systems with distinct states. J. Sound Vib. Vol. 332, No. 21 (2013), 5476–5488. DOI: 10.1016/j.jsv.2013.04.048.

[24] C. E. Lemke. Bimatrix Equilibrium Points and Mathematical Programming. Management Science Vol. 11, No. 7 (1965), 681–689. DOI: 10.1287/mnsc.11.7.681.

[25] A. Martin and F. Thouverez. Dynamic Analysis and Reduction of a Cyclic Symmetric System Subjected to Geometric Nonlinearities. J. Eng. Gas Turbines Power Vol. 141, No. 4 (2019), 041027. DOI: 10.1115/1.4041001. oai : hal-01863238.

[26] M. B. Meingast, M. Legrand, and C. Pierre. A linear complementarity problem formulation for periodic solutions to unilateral contact problems. Int. J. Non Linear Mech. Vol. 66 (2014), 18–27. DOI: 10.1016/j.ijnonlinmec.2014.01.007. oai : hal-00955647.

[27] J. J. Moreau. Unilateral Contact and Dry Friction in Finite Freedom Dynamics. *Nonsmooth Mechanics and Applications*. Ed. by J. J. Moreau and P. D. Panagiotopoulos. Vienna, 1988, pp. 1–82. DOI: 10.1007/978-3-7091-2624-0_1. oai : hal-01713847.

[28] S. Nacivet. Modélisation du frottement en pied d'aube par une approche fréquentielle. PhD thesis. École Centrale de Lyon, 2002.

[29] S. Nacivet, C. Pierre, F. Thouverez, and L. Jezequel. A dynamic Lagrangian frequency–time method for the vibration of dry-friction-damped systems. J. Sound Vib. Vol. 265, No. 1 (2003), 201–219. DOI: 10.1016/S0022-460X(02)01447-5. oai : hal-01635272.

[30] M. Nakhla and J. Vlach. A piecewise harmonic balance technique for determination of periodic response of nonlinear systems. IEEE Trans. Circuits Syst. Vol. 23, No. 2 (1976), 85–91. DOI: 10.1109/TCS.1976.1084181.

[31] B. Niedergesäß, A. Papangelo, A. Grolet, A. Vizzaccaro, F. Fontanela, L. Salles, A. Sievers, and N. Hoffmann. Experimental observations of nonlinear vibration localization in a cyclic chain of weakly coupled nonlinear oscillators. J. Sound Vib. Vol. 497 (2021), 115952. DOI: 10.1016/j.jsv.2021.115952.

[32] J. Nocedal and S. J. Wright. Numerical optimization. 2nd ed. Springer series in operations research. New York, 2006.

[33] L. Paoli and M. Schatzman. A Numerical Scheme for Impact Problems I: The One-Dimensional Case. SIAM J. Numer. Anal. Vol. 40, No. 2 (2002), 702–733. DOI: 10.1137/S0036142900378728. oai : hal-01885729.

[34] L. Paoli and M. Schatzman. A Numerical Scheme for Impact Problems II: The Multidimensional Case. SIAM J. Numer. Anal. Vol. 40, No. 2 (2002), 734–768. DOI: 10.1137/S003614290037873X.

[35] S. Patnaik, J. P. Hollkamp, and F. Semperlotti. Applications of variable-order fractional operators: a review. Proc. R. Soc. A. Vol. 476, No. 2234 (2020), 20190498. DOI: 10.1098/rspa.2019.0498.

[36] L. Peletan, S. Baguet, M. Torkhani, and G. Jacquet-Richardet. Quasi-periodic harmonic balance method for rubbing self-induced vibrations in rotor–stator dynamics. Nonlinear Dyn. Vol. 78, No. 4 (2014), 2501–2515. DOI: 10.1007/s11071-014-1606-8. oai : hal-01061265.

[37] S Pernot. A Wavelet-Balance Method to Investigate the Vibrations of Nonlinear Dynamical Systems. Nonlinear Dyn. Vol. 32 (2003), 32–70. DOI: https://doi.org/10.1023/A:1024263917587. oai : hal-00814573.

[38] E. P. Petrov. Multiharmonic Analysis of Nonlinear Whole Engine Dynamics With Bladed Disc-Casing Rubbing Contacts. *Proceedings of the ASME Turbo Expo 2012*. Vol. 7: Structures and Dynamics, Parts A and B. Copenhagen, Denmark, 2012, pp. 1181–1191. DOI: 10.1115/GT2012-68474.

[39] L. Salles, L. Blanc, F. Thouverez, A. M. Gouskov, and P. Jean. Dual Time Stepping Algorithms With the High Order Harmonic Balance Method for Contact Interfaces With Fretting-Wear. J. Eng. Gas Turbines Power Vol. 134, No. 3 (2012), 032503. DOI: 10.1115/1.4004236. oai : hal-00975699.

[40] L. Salles, A. M. Gouskov, L. Blanc, F. Thouverez, and P. Jean. Dynamic Analysis of Fretting-Wear in Joint Interface by a Multiscale Harmonic Balance Method Coupled With Explicit or Implicit Integration Schemes. *ASME Turbo Expo 2010: Power for Land, Sea, and Air*. Vol. 6: Structures and Dynamics, Parts A and B. Glasgow, UK, 2010, pp. 1003–1013. DOI: 10.1115/GT2010-23264. oai : hal-02529258.

[41] F. Schreyer and R. I. Leine. A Mixed Shooting – Harmonic Balance Method for Unilaterally Constrained Mechanical Systems. Arch. Mech. Eng. Vol. 63, No. 2 (2016), 297–314. DOI: 10.1515/meceng-2016-0017. oai : hal-01356796.

[42] G. Von Groll and D. Ewins. The harmonic balance method with arc-length continuation in rotor/stator contact problems. J. Sound Vib. Vol. 241, No. 2 (2001), 223–233. DOI: 10.1006/jsvi.2000.3298. oai : hal-01333704.

[43] L. Woiwode, N. N. Balaji, J. Kappauf, F. Tubita, L. Guillot, C. Vergez, B. Cochelin, A. Grolet, and M. Krack. Comparison of two algorithms for Harmonic Balance and path continuation. Mech. Syst. Sig. Process. Vol. 136 (2020), 106503. DOI: 10.1016/j.ymssp.2019.106503. oai : hal-02424746.

[44] J.-Y. Yoon and B. Kim. Effect and feasibility analysis of the smoothening functions for clearance-type nonlinearity in a practical driveline system. Nonlinear Dyn. Vol. 85, No. 3 (2016), 1651–1664. DOI: 10.1007/s11071-016-2784-3.

[45] C. Yoong, A. Thorin, and M. Legrand. Nonsmooth modal analysis of an elastic bar subject to a unilateral contact constraint. Nonlinear Dyn. Vol. 91, No. 4 (2018), 2453–2476. DOI: 10.1007/s11071-017-4025-9. oai : hal-01408111.

[46] S. D. Yu. An efficient computational method for vibration analysis of unsymmetric piecewise-linear dynamical systems with multiple degrees of freedom. Nonlinear Dyn. Vol. 71, No. 3 (2013), 493–504. DOI: 10.1007/s11071-012-0676-8.

[47] S. Zucca, C. M. Firrone, and M. M. Gola. Numerical assessment of friction damping at turbine blade root joints by simultaneous calculation of the static and dynamic contact loads. Nonlinear Dyn. Vol. 67, No. 3 (2012), 1943–1955. DOI: 10.1007/s11071-011-0119-y.

## A DLFT-HBM analytic jacobian

The residual expression is:

$$\mathcal{H}_{\mathrm{r}}(\widetilde{\mathbf{x}}_{\mathrm{r}}) = \mathbf{Z}_{\mathrm{r}}\widetilde{\mathbf{x}}_{\mathrm{r}} + \widetilde{\boldsymbol{\lambda}} - \widetilde{\mathbf{f}}_{\mathrm{r}} \tag{67}$$

In order to compute the full jacobian matrix associated with a continuation procedure on $\omega$, it is necessary to compute both $\dfrac{\partial \mathcal{H}_{\mathrm{r}}}{\partial \widetilde{\mathbf{x}}_{\mathrm{r}}}$ and $\dfrac{\partial \mathcal{H}_{\mathrm{r}}}{\partial \omega}$. The former reads:

$$\frac{\partial \mathcal{H}_{\mathrm{r}}}{\partial \widetilde{\mathbf{x}}_{\mathrm{r}}} = \mathbf{Z}_{\mathrm{r}} + \frac{\partial \widetilde{\boldsymbol{\lambda}}}{\partial \widetilde{\mathbf{x}}_{\mathrm{r}}} \tag{68}$$

With $\dfrac{\partial \widetilde{\boldsymbol{\lambda}}}{\partial \widetilde{\mathbf{x}}_{\mathrm{r}}}$ computed through an AFT procedure:

$$\frac{\partial \widetilde{\boldsymbol{\lambda}}_{\mathbf{x}}}{\partial \widetilde{\mathbf{x}}_{\mathrm{r}}} = -\mathbf{Z}_{\mathrm{r}} - \varepsilon\mathbf{I} \quad \text{and} \quad \left\{\frac{\partial \lambda^i}{\partial \widetilde{\mathbf{x}}_{\mathrm{r}}}\right\}_{i=1\dots N_{\mathrm{t}}} = \overline{\mathcal{F}}\frac{\partial \widetilde{\boldsymbol{\lambda}}_{\mathbf{x}}}{\partial \widetilde{\mathbf{x}}_{\mathrm{r}}} \tag{69}$$

And then the corrections are made based on the sign of $\boldsymbol{\lambda}_{\mathbf{x}}$:

$$\frac{\partial \lambda^i}{\partial \mathbf{x}_{\mathrm{r}}} = \begin{cases} \mathbf{0} & \text{if } \lambda^i_{\mathbf{x}} \leq 0 \\ \dfrac{\partial \lambda^i_{\mathbf{x}}}{\partial \widetilde{\mathbf{x}}_{\mathrm{r}}} & \text{if } \lambda^i_{\mathbf{x}} > 0 \end{cases} \quad \text{and} \quad \frac{\partial \widetilde{\boldsymbol{\lambda}}}{\partial \widetilde{\mathbf{x}}_{\mathrm{r}}} = \mathcal{F}\left\{\frac{\partial \lambda^i}{\partial \widetilde{\mathbf{x}}_{\mathrm{r}}}\right\}_{i=1\dots N_{\mathrm{t}}} \tag{70}$$

It is now necessary to compute $\dfrac{\partial \mathcal{H}_{\mathrm{r}}}{\partial \omega}$:

$$\frac{\partial \mathcal{H}_{\mathrm{r}}}{\partial \omega} = \frac{\partial \mathbf{Z}_{\mathrm{r}}}{\partial \omega}\widetilde{\mathbf{x}}_{\mathrm{r}} + \frac{\partial \widetilde{\mathbf{f}}_{\mathrm{r}}}{\partial \omega} + \frac{\partial \widetilde{\boldsymbol{\lambda}}}{\partial \omega} \tag{71}$$

The first term reads:

$$\frac{\partial \mathbf{Z}_{\mathrm{r}}}{\partial \omega}\widetilde{\mathbf{x}}_{\mathrm{r}} = -\mathbf{Z}_{\mathrm{r}}\frac{\partial\left(\left(\mathbf{Z}^1_{\mathrm{red}}\right)^{-1} + \left(\mathbf{Z}^2_{\mathrm{red}}\right)^{-1}\right)}{\partial \omega}\mathbf{Z}_{\mathrm{r}}\widetilde{\mathbf{x}}_{\mathrm{r}} \tag{72}$$

$$\frac{\partial \mathbf{Z}_{\mathrm{r}}}{\partial \omega}\widetilde{\mathbf{x}}_{\mathrm{r}} = \mathbf{Z}_{\mathrm{r}}\left(\left(\mathbf{Z}^1_{\mathrm{red}}\right)^{-1}\left[\frac{\partial \mathbf{Z}_{\mathrm{red}}}{\partial \omega}\right]^1\left(\mathbf{Z}^1_{\mathrm{red}}\right)^{-1} + \left(\mathbf{Z}^2_{\mathrm{red}}\right)^{-1}\left[\frac{\partial \mathbf{Z}_{\mathrm{red}}}{\partial \omega}\right]^2\left(\mathbf{Z}^2_{\mathrm{red}}\right)^{-1}\right)\mathbf{Z}_{\mathrm{r}}\widetilde{\mathbf{x}}_{\mathrm{r}} \tag{73}$$

As shown, it is necessary to build the $\dfrac{\partial \mathbf{Z}_{\mathrm{red}}}{\partial \omega}$ matrix prior to the calculation of $\dfrac{\partial \mathbf{Z}_{\mathrm{r}}}{\partial \omega}\widetilde{\mathbf{x}}_{\mathrm{r}}$:

$$\begin{aligned}\frac{\partial \mathbf{Z}_{\mathrm{red}}}{\partial \omega} = &\left[\frac{\partial \mathbf{Z}}{\partial \omega}\right]_{\mathrm{nl}} - \left[\frac{\partial \mathbf{Z}}{\partial \omega}\right]_{\mathrm{nl,L}}\mathbf{Z}_{\mathrm{L}}^{-1}\mathbf{Z}_{\mathrm{L,nl}} \\ &+ \mathbf{Z}_{\mathrm{nl,L}}\mathbf{Z}_{\mathrm{L}}^{-1}\left[\frac{\partial \mathbf{Z}}{\partial \omega}\right]_{\mathrm{L}}\mathbf{Z}_{\mathrm{L}}^{-1}\mathbf{Z}_{\mathrm{L,nl}} - \mathbf{Z}_{\mathrm{nl,L}}\mathbf{Z}_{\mathrm{L}}^{-1}\left[\frac{\partial \mathbf{Z}}{\partial \omega}\right]_{\mathrm{L,nl}}\end{aligned} \tag{74}$$

With the block diagonal matrix $\dfrac{\partial \mathbf{Z}}{\partial \omega}$ whose blocks $\dfrac{\partial \mathbf{Z}_k}{\partial \omega}$ are defined by:

$$\frac{\partial \mathbf{Z}_k}{\partial \omega} = \begin{pmatrix} -2k^2\omega\mathbf{M} & k\mathbf{C} \\ -k\mathbf{C} & -2k^2\omega\mathbf{M} \end{pmatrix} \quad \forall k \in [\![0, N_{\mathrm{h}}]\!] \tag{75}$$

The second term of Eq. (71) is as follows:

$$\begin{aligned}\frac{\partial \widetilde{\mathbf{f}}_{\mathrm{r}}}{\partial \omega} &= \frac{\partial \mathbf{Z}_{\mathrm{r}}}{\partial \omega}\left(\left(\mathbf{Z}^1_{\mathrm{red}}\right)^{-1}\widetilde{\mathbf{f}}^1_{\mathrm{red}} + \left(\mathbf{Z}^2_{\mathrm{red}}\right)^{-1}\widetilde{\mathbf{f}}^2_{\mathrm{red}}\right) \\ &+\mathbf{Z}_{\mathrm{r}}\left(\left(\mathbf{Z}^1_{\mathrm{red}}\right)^{-1}\left[\frac{\partial \widetilde{\mathbf{f}}_{\mathrm{red}}}{\partial \omega}\right]^1 - \left(\mathbf{Z}^1_{\mathrm{red}}\right)^{-1}\left[\frac{\partial \mathbf{Z}_{\mathrm{red}}}{\partial \omega}\right]^1\left(\mathbf{Z}^1_{\mathrm{red}}\right)^{-1}\widetilde{\mathbf{f}}^1_{\mathrm{red}}\right. \\ &\left.+\left(\mathbf{Z}^2_{\mathrm{red}}\right)^{-1}\left[\frac{\partial \widetilde{\mathbf{f}}_{\mathrm{red}}}{\partial \omega}\right]^2 - \left(\mathbf{Z}^2_{\mathrm{red}}\right)^{-1}\left[\frac{\partial \mathbf{Z}_{\mathrm{red}}}{\partial \omega}\right]^2\left(\mathbf{Z}^2_{\mathrm{red}}\right)^{-1}\widetilde{\mathbf{f}}^2_{\mathrm{red}}\right)\end{aligned} \tag{76}$$

where:

$$\frac{\partial \widetilde{\mathbf{f}}_{\mathrm{red}}}{\partial \omega} = \left(\left[\frac{\partial \mathbf{Z}}{\partial \omega}\right]_{\mathrm{nl,L}}\mathbf{Z}_{\mathrm{L}}^{-1} - \mathbf{Z}_{\mathrm{nl,L}}\mathbf{Z}_{\mathrm{L}}^{-1}\left[\frac{\partial \mathbf{Z}}{\partial \omega}\right]_{\mathrm{L}}\mathbf{Z}_{\mathrm{L}}^{-1}\right)\widetilde{\mathbf{f}}_{\mathrm{ex,L}} \tag{77}$$

The last term of Eq. (71) $\dfrac{\partial \widetilde{\boldsymbol{\lambda}}}{\partial \omega}$ is computed through an AFT procedure, as for $\dfrac{\partial \widetilde{\boldsymbol{\lambda}}}{\partial \widetilde{\mathbf{x}}_{\mathrm{r}}}$:

$$\frac{\partial \widetilde{\boldsymbol{\lambda}}_{\mathbf{x}}}{\partial \omega} = \frac{\partial \widetilde{\mathbf{f}}_{\mathrm{r}}}{\partial \omega} - \frac{\partial \mathbf{Z}_{\mathrm{r}}}{\partial \omega}\widetilde{\mathbf{x}}_{\mathrm{r}} \quad \text{and} \quad \left\{\frac{\partial \lambda^i}{\partial \omega}\right\}_{i=1\ldots N_{\mathrm{t}}} = \overline{\mathcal{F}}\frac{\partial \widetilde{\boldsymbol{\lambda}}_{\mathbf{x}}}{\partial \omega} \tag{78}$$

And then the corrections are made based on the sign of $\boldsymbol{\lambda}_{\mathbf{x}}$:

$$\frac{\partial \lambda^i}{\partial \omega} = \begin{cases} 0 & \text{if } \lambda^i_{\mathbf{x}} \leq 0 \\ \dfrac{\partial \lambda^i_{\mathbf{x}}}{\partial \omega} & \text{if } \lambda^i_{\mathbf{x}} > 0 \end{cases} \quad \text{and} \quad \frac{\partial \widetilde{\boldsymbol{\lambda}}}{\partial \omega} = \mathcal{F}\left\{\frac{\partial \lambda^i}{\partial \omega}\right\}_{i=1\ldots N_{\mathrm{t}}} \tag{79}$$